Methods for Locating Pool Liner Leakage at Nuclear Power Plants

A Review and Experimental Evaluation of Inspection Techniques for Underwater and Robotic Deployment

Nilsson, Markus

2026

Document Version:
Publisher's PDF, also known as Version of record

METHODS FOR LOCATING POOL LINER LEAKAGE AT NUCLEAR POWER PLANTS

REPORT 2026:1156

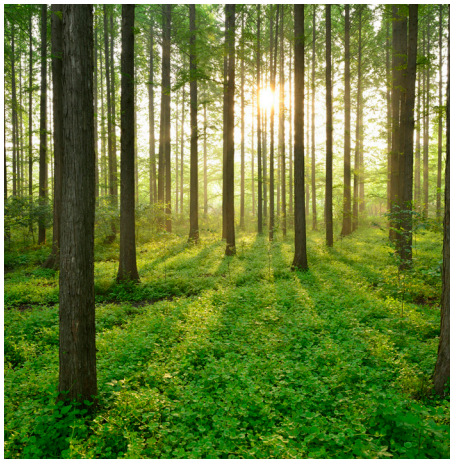

NUCLEAR POWER
CONCRETE TECHNOLOGY

Energiforsk

Methods for Locating Pool Liner Leakage at Nuclear Power Plants

A Review and Experimental Evaluation of Inspection Techniques for Underwater and Robotic Deployment

MARKUS NILSSON

ISBN 978-91-89917-03-3 | © Energiforsk January 2026

Energiforsk AB | Phone: 08-677 25 30 | E-mail: kontakt@energiforsk.se | www.energiforsk.se

Foreword

This report forms the results of a project performed within the Energiforsk Nuclear Power Concrete Program

The Concrete Program aims to increase the knowledge of aspects affecting safety, maintenance and development of concrete structures in the Nordic nuclear power plants. A part of this is to investigate possibilities to facilitate and simplify the work that is performed in the nuclear business.

Detection and repair of leakages in pool liners at nuclear power plants poses significant challenges. Addressing this issue is important to minimize radiation to personnel as well as operational downtime.

This study evaluates advanced non-destructive testing (NDT) methods for detecting and localizing leakage-relevant defects in thin austenitic stainless-steel liners. It also explores robotic manipulators for underwater inspections, aiming to reduce downtime and improve inspection efficiency.

The findings highlight Alternating Current Field Measurement (ACFM) as the most promising technique for surface-breaking cracks, with several other methods offering complementary capabilities. Practical recommendations for robotic deployment and multimodal inspection strategies are provided to enhance nuclear pool liner integrity.

The study was carried out by Markus Nilsson, Faculty of Engineering, Lund University. The study was performed within the Energiforsk Concrete Program, which is financed by Vattenfall, Uniper, Fortum, TVO, Skellefteå Kraft, Karlstads Energi, the Swedish Radiation Safety Authority and SKB.

These are the results and conclusions of a project, which is part of a research Program run by Energiforsk. The author/authors are responsible for the content.

Cover image: Reactor basin at Oskarshamn 3 nuclear power plant. Image courtesy of OKG AB.

Summary

This report addresses the challenge of localizing leakage-relevant defects in thin austenitic stainless-steel pool liners at nuclear power plants, with particular emphasis on inspections performed under water and under access-limited conditions. The work combines a state-of-the-art review of non-destructive testing (NDT) techniques and robotic deployment concepts with targeted experimental investigations, aiming to assess both technical capability and practical applicability.

The literature review evaluates mechanical wave-based, electromagnetic, and visual inspection methods with respect to defect sensitivity, robustness in submerged environments, compatibility with robotic platforms, and suitability for detecting surface-breaking defects relevant to leakage. Electromagnetic techniques, in particular Alternating Current Field Measurement (ACFM), are identified as well aligned with the characteristics of leakage-relevant cracks due to their high surface sensitivity, tolerance to lift-off and coatings, and demonstrated performance in underwater and nuclear environments. Phased Array Ultrasonic Testing (PAUT) offers complementary capabilities where quantitative imaging, weld interrogation, or more detailed defect characterization is required. Visual inspection and photogrammetry provide efficient screening and documentation but lack depth information, while Acoustic Emission and conventional eddy current techniques are assessed as less suitable for direct leakage localization in this application.

To support and contextualize the review, controlled experiments were performed on a 3 mm EN 1.4307 (304L) stainless-steel plate in both free and concrete-bonded configurations, focusing on shear-horizontal (SH) guided waves generated using electromagnetic acoustic transducers (EMATs). The experiments demonstrate that SH0 waves at 600 kHz enable stable, couplant-free transmission measurements and can detect narrow, elongated artificial defects under controlled conditions. The results clarify how defect orientation, polarization, mode content, and boundary conditions influence detectability, while also highlighting practical limitations in achievable resolution for very small defects. The experiments are intended to elucidate detection mechanisms and scanning behaviour rather than to establish absolute detection limits for the smallest possible leaks.

Based on the combined findings, the report concludes that effective leakage localization in nuclear pool liners requires a pragmatic, deployment-oriented approach. ACFM is recommended as the primary near-term technique for underwater localization of surface-breaking cracks in thin liners, with PAUT applied selectively where additional characterization is needed. Visual inspection and photogrammetry should be used to guide and contextualize targeted NDT, while other techniques may contribute in complementary or supporting roles. Together, the results provide a clear basis for prioritizing inspection methods and for planning future development toward more reliable and efficient leakage localization with reduced operational impact.

Keywords

Spent fuel pools (bränslebassänger); leakage localization (läckagelokalisering); NDT (icke-förstörande provning); ACFM (Alternating Current Field Measurement); PAUT / Phased Array Ultrasonic Testing; Acoustic Emission (akustisk emission); Visual testing & photogrammetry (visuell provning och fotogrammetri); EMAT (Elektromagnetisk akustisk sökare); SH guided waves; Stainless steel liners (rostfri tätplåt)

Sammanfattning

Denna rapport behandlar problematiken kring lokalisering av läckagerelaterade defekter i tunna austenitiska rostfria tätplåtar i kärntekniska bassänger, med särskilt fokus på inspektion under vatten och vid begränsad åtkomlighet. Arbetet kombinerar en översikt av aktuell kunskapsnivå inom icke-förstörande provning och robotiserad inspektion med riktade experiment, i syfte att bedöma både teknisk potential och praktisk tillämpbarhet.

Litteraturstudien analyserar mekaniska vågmetoder, elektromagnetiska metoder samt visuella inspektionsmetoder utifrån deras känslighet för relevanta defekttyper, robusthet i undervattensmiljö, kompatibilitet med robotplattformar och möjligheter till praktisk användning i kärntekniska bassänger. Elektromagnetiska metoder, särskilt Alternating Current Field Measurement (ACFM), bedöms vara väl anpassade för lokalisering av ytöppna sprickor som är relevanta för läckage, tack vare hög ytkänslighet, tolerans mot lyftavstånd och beläggningar samt dokumenterad användning i undervattens- och kärntekniska tillämpningar. Phased Array Ultrasonic Testing (PAUT) erbjuder kompletterande möjligheter där kvantitativ avbildning, svetsgranskning eller fördjupad defektkarakterisering krävs. Visuell inspektion och fotogrammetri är effektiva för screening och dokumentation men saknar djupinformation, medan akustisk emission och konventionell virvelströmsprovning bedöms vara mindre lämpade för direkt lokalisering av etablerade läckage i denna tillämpning.

För att förankra litteraturöversiktens slutsatser genomfördes kontrollerade experiment på en 3 mm tjock plåt av EN 1.4307 (304L), både som fri plåt och med plåten kopplad mot betong. Försöken fokuserade på skjuvhorisontella (SH) styrda vågor genererade med elektromagnetiska akustiska givare (EMAT). Resultaten visar att SH0-vågor vid 600 kHz möjliggör stabila, kopplingsfria transmissionsmätningar och kan detektera smala, långsträckta defekter under kontrollerade förhållanden. Samtidigt tydliggör försöken hur defektorientering, vågpolarisation, modinnehåll och randvillkor påverkar detekterbarheten, samt vilka begränsningar som finns för mycket små defekter. Experimenten syftar till att klargöra mekanismer och skanningsbeteende snarare än att fastställa absoluta detektionsgränser.

Sammantaget visar resultaten att effektiv läckagelokalisering i kärntekniska bassänger kräver en praktiskt orienterad och genomförbar inspektionsstrategi. ACFM rekommenderas som primär metod för undervattenslokalisering av ytöppna sprickor i tunna tätplåtar, med PAUT som ett selektivt komplement för vidare karaktärisering. Visuell inspektion och fotogrammetri bör användas som stöd för riktad provning genom screening och dokumentation. Rapporten ger därmed ett tydligt underlag för prioritering av metoder och för fortsatt utveckling mot mer tillförlitlig och effektiv läckagelokalisering med begränsad påverkan på drift.

List of content

1 Introduction

Nuclear power plants (NPPs) consist of multiple concrete structures that are essential for both safety and operation. Among these structures are various pools (or basins) with distinct functions. Examples include spent nuclear fuel (SNF) pools, which store used fuel, and condensation basins (wet-well), which are integral to the safety systems of boiling water reactors (BWRs) in case of an accident. Both types of pools are critical for the safe operation of an NPP.

The pools are constructed of reinforced concrete, clad with a welded stainless steel liner designed to ensure leak tightness. A significant leak, such as one caused by a defect in the liner, could have severe implications for reactor safety. Additionally, such leaks could lead to substantial economic consequences, as the reactor would need to be taken offline until the issue is resolved.

At several facilities, minor leaks have been detected in the lower sections of the containment structure. These leaks have been traced back to the pools within the containment. Beyond the direct loss of water, leaks also increase the risk of corrosion in embedded steel components, such as reinforcement bars, and other embedded metallic elements.

A key challenge when a leak is suspected is pinpointing its exact location. The total surface area of the pool walls and floor is extensive, and even minor defects can, over time, lead to significant leakage. To detect leaks, leakage monitoring channels are located near the liner welds (see Figure 2). These channels facilitate a rough approximation of the leak's origin. However, accurately locating leaks requires draining and cleaning the pools. Such procedures are both time-consuming and feasible only when the reactor is offline. Once drained, personnel must conduct manual inspections to pinpoint the exact source of the leakage. The inspection procedures vary from

visual and penetrant testing to eddy current testing and ultrasonic examination. Given these constraints, there is a strong need for a methodology that enables leak localization without draining the pool.

Although a wide range of non-destructive testing (NDT) techniques exists for defect detection in metallic structures, relatively few have been demonstrated to work reliably under the combined constraints of thin austenitic stainless steel, submerged conditions, limited accessibility, and robotic deployment. As a result, leakage localization in pool liners remains challenging in practice despite the apparent availability of inspection technologies.

This report is written for technical professionals involved in inspection, maintenance, or research related to nuclear power plant pool structures. While some familiarity with NDT principles is assumed, the presentation aims to remain accessible to readers with general engineering backgrounds. Key concepts are introduced as needed to ensure readability for non-specialists.

The objective of this report is to provide a structured assessment of inspection methods and deployment concepts relevant for leakage localization in nuclear pool liners, with the aim of supporting method selection, prioritization, and future development toward practical in-situ application. The work does not seek to define absolute detection limits for the smallest possible leaks, but rather to evaluate practical capabilities, limitations, and trade-offs under realistic operating conditions. In addition, the report considers the role of remotely operated vehicles (ROVs) and similar platforms for performing NDT in submerged environments. The findings are synthesized into application-oriented recommendations to guide future studies and inspection planning.

2 Pool Liners in Nuclear Power Plants

The most common type of nuclear reactors worldwide is so-called Light Water Reactors (LWRs). The two main types of LWRs are Pressurized Water Reactors (PWRs) and Boiling Water Reactors (BWRs). As the names suggest, their operating principle varies in how the light water is used for generating electricity.

In Pressurized Water Reactors (PWRs), water is kept under high pressure to prevent boiling as it circulates through the reactor core. The heat from the reactor is transferred to a secondary loop, where steam is generated to drive a turbine and produce electricity. Boiling Water Reactors (BWRs), on the other hand, allow water to boil directly in the reactor core, generating steam that is sent directly to the turbine. A reactor basin in a BWR plant is shown in Figure 1, illustrating the pool environment nuclear power plants (image courtesy of OKG AB).

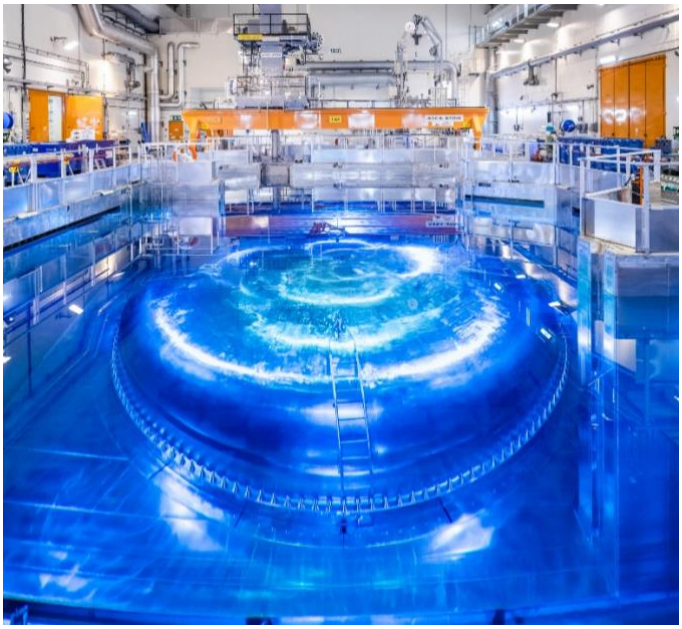

Figure 1. Reactor basin in a BWR plant, Oskarshamn 3. Source: OKG AB.

A critical component of nuclear reactor safety is the pool liner used in spent nuclear fuel pools. These pools store and cool used nuclear fuel after it is removed from the reactor. Additionally, condensation basin liners are essential for managing excess steam and water during

reactor operations and emergency cooling scenarios in BWR operations. These basins collect condensed steam and cooling water, preventing uncontrolled releases into the environment. Austenitic stainless-steel liners are commonly used for both pool liners due to their high corrosion resistance, durability, and welding properties [1].

Various types of pool liners ensure structural integrity and prevent leakage of radioactive materials by maintaining a leak tight barrier to the surrounding concrete structure. It is therefore critical that the structural integrity of the pool liners is ensured and that any breach of leak tightness is detected, localized, and remedied. Figure 2 shows the design of a pool liner in a spent fuel pool in a Swedish PWR. The pool liners are rectangular pieces with a thickness of 3–4 mm, and they are welded together and anchored to the concrete, for example by a concrete-embedded L-profile (Figure 2). Leakage monitoring channels are employed near the welds to facilitate the *detection* of leaks.

Pool liners cover a substantial surface area, which truly makes *locating* leakages challenging. Although, leakage monitoring channels give an indication into which region detailed efforts should be focused on. To locate the leaks, the pools must be drained and sanitized before personnel can perform the inspections. However, an estimate of the vertical position of the leakage can be approximately determined by gradually lowering the water level until the liner ceases to leak.

In current practice, the inspection is primarily carried out through visual testing in combination with liquid penetrant testing. In this method, a fluorescent penetrant is applied to the liner surface and allowed to seep into surface-breaking defects. After the surface is cleaned, excess penetrant is removed while penetrant trapped in the defect remains visible under UV light, enabling clear visual indications. Other industrially employed leak testing methods include tracer gas-based methods, such as accumulation testing and local sniffing tests, and bubble emission techniques [2].

While effective for detecting surface-breaking flaws and active leaks, these methods require full pool drainage, thorough cleaning, and direct human access, making the localization of leaks a time-consuming and resource-intensive operation. Other non-destructive techniques such as eddy current testing and ultrasonic examination are also employed at some facilities, but to a much lesser extent

compared to visual and penetrant testing, as they require more specialized equipment and certified personnel.

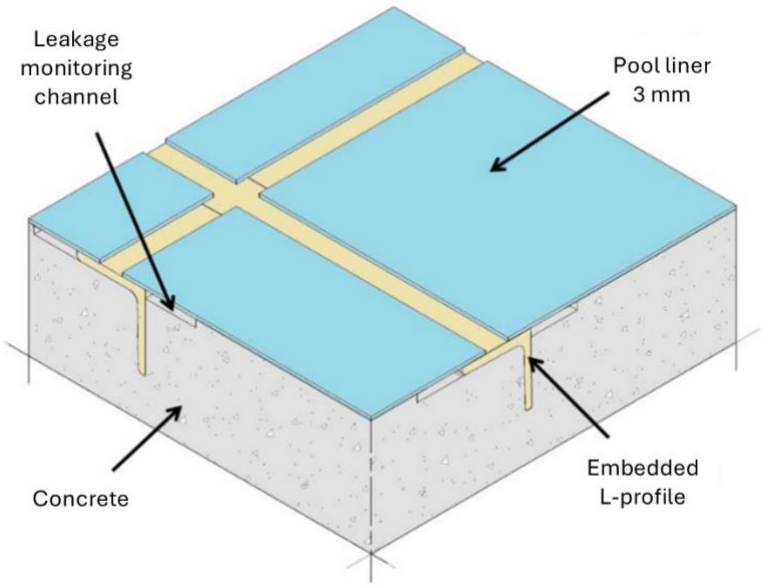

Figure 2. Illustration of the pool liner and related components.

Some nuclear facilities have incorporated magnetite aggregates in the concrete structures to improve their ability to withstand radiation and high temperatures. While effective for structural and shielding purposes, these ferromagnetic inclusions can introduce local electromagnetic anomalies, potentially interfering with electromagnetic NDT methods by distorting magnetic fields or affecting signal consistency near the liner surface.

These challenges highlight the need for improved, remotely deployable NDT methods that can localize leakage-relevant defects without draining the pools or relying solely on surface-access methods such as visual and penetrant testing. Developing suitable techniques, instrumentation, and manipulators would significantly reduce downtime, radiation exposure, and the operational costs associated with current inspection practices.

2.1 CHALLENGES WITH AUSTENITIC STAINLESS-STEEL LINERS

Austenitic stainless steels, particularly grades such as AISI 304L (EN 1.4307/SS2352) and AISI 316L (EN 1.4436/SS2343), are widely used in nuclear pool liners due to their excellent corrosion resistance,

weldability, and durability in submerged environments [1]. However, their material properties pose several challenges for NDT.

One of the primary challenges arises from the coarse grain structure typical for austenitic stainless steel, especially in welded areas. The grain size can be significantly larger than in ferritic steels, which is illustrated in Figure 3. This results in strong scattering and attenuation of acoustic waves at high frequencies (several MHz), reducing the signal-to-noise ratio and complicating flaw detection. Due to its grain structure, austenitic steel exhibits variable degrees of anisotropy [3]. This complicates elastic wave propagation further, particularly in welds [4]. Austenitic steels are nonmagnetic in annealed condition but can become slightly magnetic when cold worked, e.g., by rolling [5]. The variability in electric and magnetic properties due to cold working could affect the application of electromagnetic methods [6].

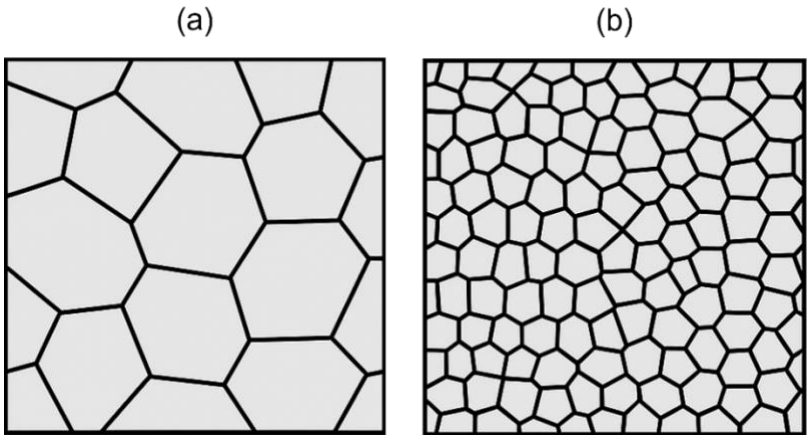

Figure 3. Grain structure for (a) austenitic steel and (b) ferritic steel.

Small observed leakage rates in pool liners are often associated with very small equivalent hydraulic openings, sometimes expressed as sub-millimetre circular apertures inferred from hydrostatic considerations. Such estimates represent effective flow areas rather than the true geometric characteristics of leakage-relevant defects. This distinction complicates both the detection and localization of leakage-relevant defects, as small leakage rates do not directly translate to simple or easily detectable defect geometries.

Welded joints present a significant challenge. The fusion zone and heat-affected zone exhibit heterogeneous grain structures and variable mechanical properties, which contribute to inconsistent mechanical wave propagation and increased attenuation. Moreover, welded

regions in austenitic stainless steel are particularly susceptible to stress-corrosion cracking (SCC), a failure mechanism that arises from the combined effects of tensile stress and a corrosive environment [7]. SCC can initiate and propagate along grain boundaries or through the grains, often with little warning, making early detection and characterization challenging. In addition, austenitic stainless steels can suffer from intergranular corrosion, especially in the heat-affected zone when sensitization occurs [7]. This localized form of corrosion follows grain boundaries, potentially weakening weld integrity which may ultimately lead to leakage.

Dissimilar metal welds. which are used to join austenitic stainless steels to other materials, such as the L-profiles illustrated in Figure 2, introduce additional complications. These welds often feature abrupt changes in microstructure and mechanical properties across the interface, increasing the likelihood of residual stress concentrations, localized corrosion, and crack initiation.

The most critical areas susceptible to degradation and damage in austenitic stainless-steel pool liners are therefore suspected to be the welded joints, structural corners, and dissimilar metal weld interfaces. These regions tend to accumulate mechanical and thermal stress and often exhibit complex geometries that cause local weakening. As a result, these locations are not only more likely to develop cracks or corrosion but are also more difficult to inspect reliably.

The inspection of austenitic stainless-steel pool liners is complicated by the material's microstructure, weld characteristics, and geometric conditions. These inherent material features and geometric challenges must be considered when evaluating the effectiveness of any non-destructive inspection approach.

3 Leakage Localization Methods

Locating leakage in stainless-steel pool liners requires non-destructive testing (NDT) methods with sufficient spatial resolution to identify the actual defect in the steel plate. Although leakage monitoring channels are installed behind the liner, these channels only detect that water has entered the system and can at best indicate a coarse region where the leak may originate. A single channel may extend over several meters of welds or plate panels, meaning that it provides detection without localization. Accurate localization must therefore rely on complementary NDT techniques.

In current practice, effective localization is typically achieved only after the pool has been drained and cleaned, allowing personnel to perform manual inspections such as visual testing and liquid penetrant examination of welds, corners, and plate surfaces. This approach provides good sensitivity to surface-breaking defects, but is resource-intensive, requires extensive sanitizing, and results in extended downtime.

In addition, several established leak testing methods exist for leakage verification. The European standard EN 1779 Annex A describes leak testing techniques, including tracer gas-based methods such as accumulation testing (Technique B3) and local sniffing tests (Technique B4), as well as bubble emission techniques using vacuum box testing (Technique C3) [2]. These methods are widely used in industrial leak testing and offer high sensitivity to through-wall leakage. Comparable tracer-gas sniffing approaches are also described in the ASME Boiler and Pressure Vessel Code, Section V, Article 10, Appendix 4, using helium mass spectrometer detector probe techniques.

While these techniques are effective for confirming the presence of leakage, they generally require pressurization, tracer-gas handling, enclosure, or dry access to the inspected surface. For large, extended liner structures submerged in water, their spatial coverage is limited, and practical application typically requires draining or isolating the structure.

Another practical way to estimate the vertical position of a leakage source is to gradually lower the water level until the leakage stops. Taken together, these approaches can confirm leakage and provide coarse localization. However, no established in-situ method has been identified for reliably locating leakage sources under water in operating pool environments.

The aim of this report is therefore to evaluate NDT techniques that could enable remote, underwater localization of leakage-relevant defects in thin austenitic stainless-steel liners. The target application is not continuous monitoring or early crack initiation detection but rather finding the defect responsible for an observed leak, without the need to drain the pool. Such a method must be able to:

- Be sensitive enough to detect small defects, as even minor flaws in pool liners can lead to significant leakage.
- Precisely *locate* defects, rather than merely detecting their presence.
- They should be suitable for inspecting thin plates, which requires high-resolution techniques.
- The methods should be suitable for automated underwater applications.

The scope therefore encompasses the entire liner surface, including welds, heat-affected zones, corners, attachments, and regions where the plate is constrained by concrete or steel profiles. While welds are expected to be the most susceptible areas, defects may occur anywhere along the liner. For this reason, both weld-focused and plate-focused NDT methods are evaluated.

The following sections review relevant NDT techniques grouped by their governing physical principles: mechanical waves, electromagnetic methods, and optical approaches, emphasizing their applicability for underwater, remote inspection of stainless-steel pool liners.

3.1 MECHANICAL WAVE METHODS

When sound travels through a medium such as air or steel, it disturbs the particles within, causing them to oscillate around their equilibrium positions. These oscillations transfer energy through

collisions or interactions with neighbouring particles, facilitating the propagation of *mechanical* waves. The perturbation is characterized by its amplitude, which defines the strength of the disturbance; its frequency, which describes how fast the oscillation occurs; and its wavelength, which represents the spatial extent of the oscillation. The wavelength is governed by the frequency and the speed of sound in the medium in which the wave propagates.

For NDT, the wavelength plays a critical role as it typically governs which defects can be detected. Generally, if a defect is much smaller than the probing wavelength, it cannot be detected. It is therefore crucial to consider the wavelength in the application of ultrasound.

Another important aspect of mechanical waves is their polarization, which describes the nature of particle displacement relative to the wave's direction of propagation. *Bulk waves* travel through the volume of a material and can be classified as *longitudinal* waves, where particles oscillate in the same direction as wave propagation, or *transverse* waves, where displacement occurs perpendicular to the propagation direction.

In contrast, *guided waves* are mechanical waves that propagate within a structure, such as a thin plate, pipe, or layered material, where the boundaries constrain their motion. These waves exhibit complex displacement patterns, combining both longitudinal and transverse motion depending on the wave mode.

Given the vast number of mechanical wave-based NDT methods, this report focuses on the following techniques:

- *Guided Wave Testing* (GWT) – typically effective for long-range inspection along thin structures.
- *Phased Array Ultrasonic Testing* (PAUT) – enables detailed imaging and precise flaw characterization.
- *Acoustic Emission (AE)* – enables continuous monitoring of crack initiation, propagation, and localization of events.

While Time-of-Flight Diffraction (TOFD) is an established method for detecting and sizing planar flaws in thick components [8], it is not well-suited for locating through-wall cracks that would be required for leakage to occur. Similarly, nonlinear ultrasonic techniques have shown promise in detecting early-stage microstructural damage in metals [9]. However, their applicability to leakage localization is

limited since TOFD relies on diffraction due to crack tips and nonlinear ultrasonics are mainly sensitive to partial bonds in cracks and stress concentrations in crack tips. These highly capable classes of mechanical wave-based NDT methods will therefore not be emphasized in this report, although they should still be considered valuable for detecting precursors to leakage in broader structural integrity assessments.

The following sections present the state-of-the-art for each method mentioned in the list above, focusing on weld and corrosion inspection, as well as their potential for automated underwater application.

3.1.1 Guided Wave Testing

Introduction to Guided Waves

Mechanical waves that are constrained by the geometric boundary of the medium in which they propagate are called *guided waves*. Common types of guided waves include Lamb waves, which propagate in thin plates with symmetric or antisymmetric displacement modes that are both parallel and perpendicular to the propagation direction (see Figure 4) [10], and shear horizontal (SH) waves, where particle motion is purely transverse [11]. Because guided waves can travel long distances with minimal energy loss, they are widely used in non-destructive testing (NDT) for detecting defects in engineering structures such as pipelines, aircraft, and composite materials [12].

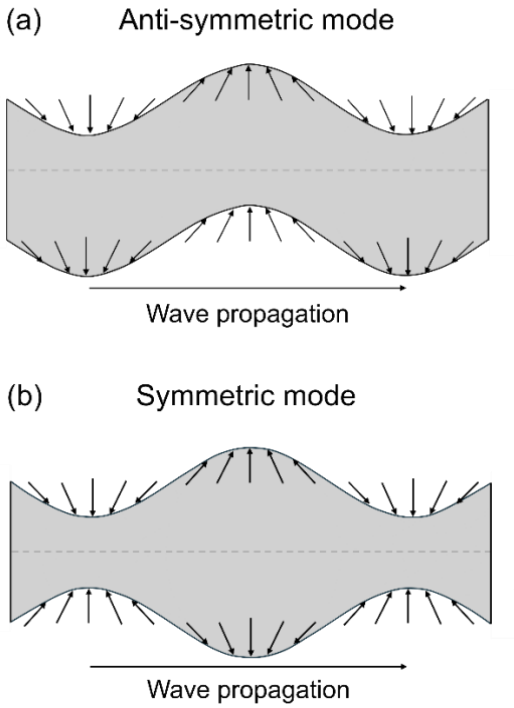

Figure 4. Illustration of guided Lamb wave modes in a plate. (a) Anti-symmetric mode and (b) symmetric mode. The dashed line indicates plate center.

Lamb waves require free or partially free boundaries to propagate. A concrete-bonded liner heavily constrains one side, thus absorbing energy and suppress wave modes, specifically antisymmetric modes. This induces strong attenuation and mode conversions which make the analysis complex [13]. This makes the use of Lamb waves limited for pool liner inspection.

An alternative leaky guided wave that has been proposed for use in NDT of fluid-filled tanks and pipes is the quasi-Scholte (QS) wave [14]. QS waves propagate along the fluid-solid interface with minimal attenuation due to leakage which makes them promising for fluid-filled tank and pipe inspection. However, their applicability in the context of a water-steel-concrete system such as the NPP pool liners remains uncertain, as the steel-concrete interface is likely to restrict or attenuate QS modes. Additionally, the excitation and detection of QS waves in multilayered, constrained geometries can be challenging, and their sensitivity to defects in such configurations is not yet well established. This motivates the exploration of alternative wave modes,

such as shear horizontal (SH) waves, which may offer more favourable propagation characteristics under these conditions.

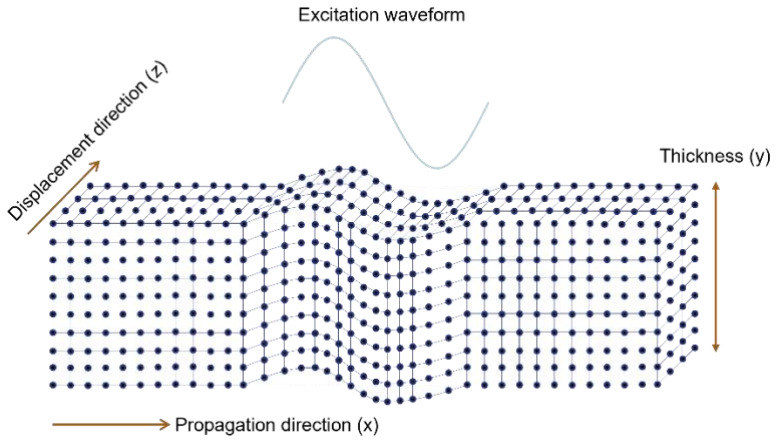

Figure 5. Illustration of a horizontally polarized shear wave with unidirectional displacement in the z-direction and propagation in the x-direction. No excitation is applied in the y-direction. Figure reproduced from [15].

SH guided waves are not significantly affected by fluid or solid interfaces, as their particle displacement is strictly transverse to the direction of propagation and lies entirely within the plane of the plate, as illustrated in Figure 5. The transverse particle displacement makes them less susceptible to energy leakage into adjacent media, such as water. However, as with any guided wave, SH-waves are still affected by the apparent change of geometry due to factors such as welded contacts to other elements, or concrete bond. Any contact will affect the propagating modes. SH-waves have additional benefits for austenitic steel inspection as they attenuate less and do not experience mode conversion at coarse grain boundaries or welds parallel to the polarization (z in Figure 5) [16, 17].

An important consideration regarding guided waves is their *dispersion* behaviour, meaning that different frequencies and modes propagate at different velocities. Dispersion is generally described in two quantities: the *phase* and *group* velocities. The phase velocity defines the speed at which individual wave phases (or crests) travel, whereas the group velocity corresponds to the speed of a wave packet (envelope).

The reason why it is important to consider dispersion is that the simultaneous excitation of multiple modes or frequencies can lead to multi-mode interference which may result in signal distortion and

loss of spatial resolution. This effect complicates the interpretation of received signals and can reduce defect localization accuracy.

An interesting property of SH-waves is that fundamental SH-mode (SH0) is *non-dispersive* in a free plate or half-space. This means that its phase- and group velocity is equal to the bulk shear velocity (c_s). In contrast, higher-order modes (SH1, SH2, ...) are dispersive and only exist above their respective cutoff frequencies. Figure 6 shows the phase- (a) and group velocity (b) curves [18] for the first four SH modes in a 3 mm thick plate with a shear velocity of c_s. The SH0 mode remains constant at c_s, while the higher modes exhibit increasingly strong dispersion near their cutoff frequencies before asymptotically approaching c_s at higher frequency–thickness values.

For SH waves in a plate, the through-thickness displacement is given by [18]:

$$\mathbf{u_y}(\boldsymbol{z}) \propto \begin{cases} \boldsymbol{cos}\left(\dfrac{\boldsymbol{m\pi z}}{\boldsymbol{2h}}\right), \boldsymbol{m} = \mathbf{0}, \mathbf{2}, \mathbf{4}, \ldots \\ \boldsymbol{sin}\left(\dfrac{\boldsymbol{n\pi z}}{\boldsymbol{2h}}\right), \boldsymbol{n} = \mathbf{1}, \mathbf{3}, \mathbf{5}, \ldots \end{cases} \quad (1)$$

where m and n are the mode order of the even and odd modes, respectively. The plate thickness is represented by $2h$. Thus, SH0 ($m = 0$) has a constant displacement through the thickness, whereas SH1 ($n = 1$) contains a nodal plane at $z = 0$. Figure 6 (c) illustrates the corresponding through-thickness displacement shapes for SH0 and SH1, highlighting the uniform in-plane shear of the fundamental mode and the alternating displacement direction introduced by the first higher-order mode.

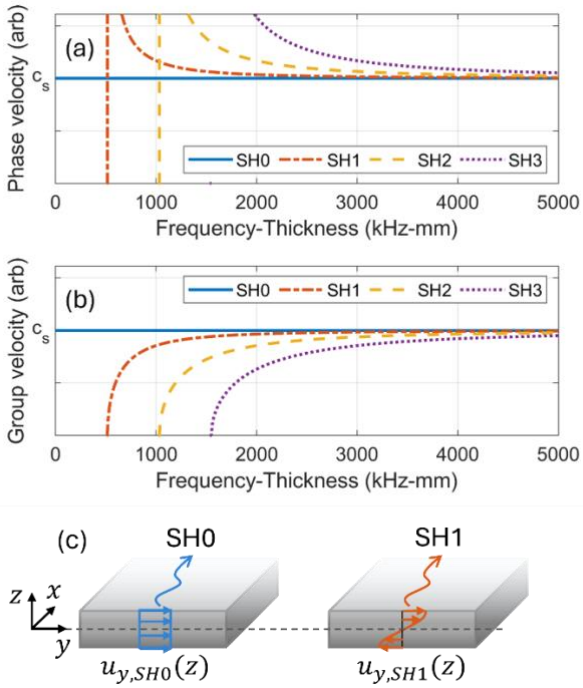

Figure 6. Dispersion curves for shear-horizontal (SH) guided waves in a 3 mm stainless-steel plate. (a) Phase velocity and (b) group velocity as functions of frequency–thickness. (c) Corresponding through-thickness displacement (mode) shapes $u_y(z)$ for SH0 and SH1.

Generation of Horizontal Shear (SH) Waves

There are practical limitations when it comes to generating SH waves in an underwater environment. Standard piezoelectric transducers must be coupled to the liner by some viscous substance, such as hot glue, silicone grease, or special shear wave couplants [19], to enable the efficient transfer of transverse waves. This is illustrated in Figure 7. Applying and maintaining such a coupling agent under water is impractical, particularly for large-scale or automated inspections. The solution can be to introduce the SH-waves using electromagnetic fields.

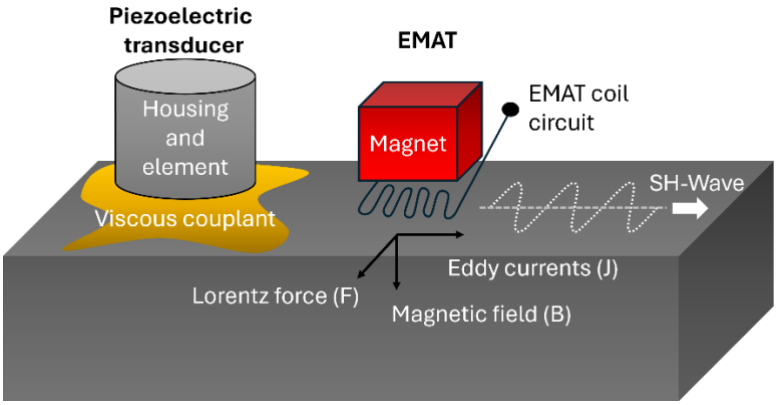

Figure 7. Illustration of a standard piezoelectric transducer compared to an EMAT.

Efficiently transferring guided waves into a steel plate under water can be achieved by using state-of-the-art electromagnetic acoustic transducers (EMATs) [20]. These transducers generate ultrasound within a conductive material by utilizing both an oscillating magnetic field at an ultrasonic frequency and a static magnetic field. The alternating magnetic field induces eddy currents (J) in the material, which interact with the static field (B), generating a Lorentz force ($F = JxB$). This force directly excites mechanical vibrations within the material, producing ultrasonic waves [21]. When an acoustic wave reaches an EMAT, the coil is perturbed and so is the magnetic field, which is then measured. A simple illustration of an EMAT compared to a standard transducer is shown in Figure 7 where it is shown how the Lorentz force induces SH-waves. The principle is illustrated in further detail in Figure 8. EMATs do not require a couplant or direct contact with the subject under test which makes the generation of SH-waves more feasible in underwater scenarios.

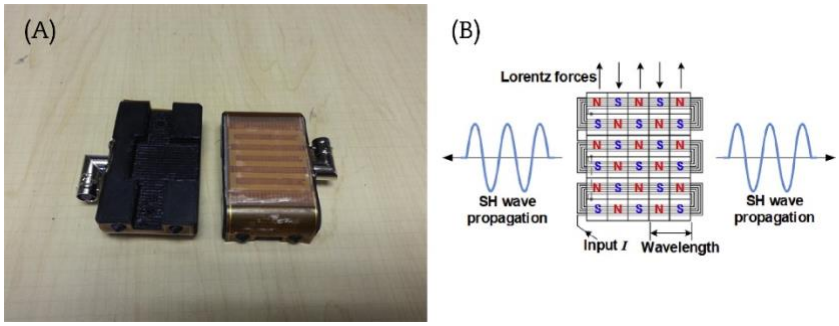

Figure 8. Electromagnetic acoustic transducers (EMATs) to send and receive shear-horizontal (SH) waves. (A) Pair of compact periodic permanent magnet EMATs. (B) Schematic diagram of the SH wave generation mechanism by Lorentz forces. Adapted from Choi et al. [22], licensed under CC BY-NC-ND 4.0.

A drawback of EMATs in underwater applications is their sensitivity to lift-off, i.e., the varied distance from the EMAT to the specimen surface, which can result in inconsistent signal quality. This issue is particularly critical when EMATs are mounted on remotely operated vehicles, where precise control of standoff distance is difficult. Magnetic attraction between the EMAT and the steel surface can introduce pull-back forces that destabilize the scanning head, further complicating consistent coupling and data acquisition. Additionally, EMATs typically require higher input power than traditional piezoelectric transducers.

Applications of EMAT SH-wave Inspection of Austenitic Stainless Steel

One concern with EMAT SH inspection of austenitic steel is the material's low conductivity and magnetism. However, Gao et al. [16] successfully used EMAT generated SH waves to detect defects as small as 0.5 mm in 25 mm thick austenitic welds, demonstrating effective single-sided inspection despite the limitations posed by the material. P.A. Petcher and S. Dixon [17] demonstrated successful inspection of 316L stainless steel welded plates containing a range of artificial defects, including cracks and lack of fusion using periodic permanent magnet (PPM) EMATs. The method showed high sensitivity and consistent defect detection from all inspection sides, outperforming conventional piezoelectric phased array techniques in this context. Choi et al. [23] developed temperature- and radiation-tolerant SH-wave EMATs which were successfully applied for detecting surface-breaking defects in 304 stainless steel welded plates under simulated dry cask storage conditions using robotic manipulators. These EMATs were specifically designed to operate in harsh environments, withstanding temperatures up to 177 °C and gamma radiation doses up to 5920 krad, while maintaining effective sensitivity to notches in welded areas [23].

These reported applications demonstrate the applicability of SH-wave inspection using EMATs for surface-breaking defects in austenitic steel – precisely the type of flaws most critical for leakage localization. This effectiveness is likely due to the particle displacement of SH-waves being confined to the plane of the plate, enhancing sensitivity to surface and near-surface anomalies while minimizing energy leakage into surrounding media. Combined with the non-contact, couplant-free nature of EMATs, SH-wave inspection offers a promising solution for evaluating thin austenitic stainless-steel liners

in submerged and access-limited nuclear environments. Although direct experimental studies on thin plate inspection are limited, recent numerical investigations by Saitoh and Ishiguro [24] have demonstrated the viability of SH guided waves for detecting surface-breaking cracks in thin plates using advanced methods such as time reversal analysis and topological sensitivity.

While SH-wave EMAT inspection shows strong potential for locating leakage-relevant defects in pool liners, several areas remain open for future research. Most notably, experimental validation of detection and classification capabilities for through-wall cracks (active leaks), as well as near-surface and surface-breaking cracks (potential leakage initiators), in thin liners is needed. The inspection of complex geometries such as corners and weld junctions warrants further exploration.

One inherent limitation that requires further investigation is the practical spatial resolution achievable in thin (~3 mm) liners. Because the SH0 mode is non-dispersive, its wavelength can only be reduced by increasing frequency. However, in thin plates the cutoff frequencies of higher-order SH modes lie relatively low, meaning that increasing frequency quickly introduces additional dispersive modes (SH1, SH2, …). These modes overlap with SH0 and complicate interpretation, while attenuation also increases with frequency. As a result, there is an upper practical limit on usable frequency and therefore on the minimum resolvable defect size. How this trade-off affects detection of small, leakage-relevant defects in thin liners remains an important topic for experimental validation.

Additionally, practical implementation in submerged environments will depend on advancements in robotic or ROV-based EMAT manipulation systems, where challenges related to precise positioning, lift-off control, underwater stability, and access to high-power pulsers remain to be addressed.

3.1.2 Phased Array Ultrasonic Testing (PAUT)

Introduction to PAUT

Conventional ultrasonic testing relies on using single-element transducers to transmit and receive acoustic waves. This setup limits the inspection to a fixed beam angle and focal depth, making it difficult to thoroughly scan welds, corners, or complex geometries.

The beam angle is governed by the wedge used, and inspecting with multiple angles typically requires physically changing wedges. This makes the process time-consuming and increases the risk of missing defects due to limited coverage. This limitation is especially problematic in austenitic stainless steel, where a fixed beam path using longitudinal waves may be insufficient for reliable defect detection due to wave attenuation, scattering, and anisotropy [4].

To overcome these limitations, phased array (PA) transducers have been developed, incorporating multiple individually controlled elements and beamforming electronics. By introducing time delays between the excitation of each element, the resulting wavefront can be steered and focused electronically. As illustrated in Figure 9, a phased array enables sweeping of beam angles from a single probe position, significantly enhancing inspection coverage and defect detectability without the need to change the wedge. Phased Array Ultrasonic Testing (PAUT) has therefore developed into a widely used technology for weld inspection [25].

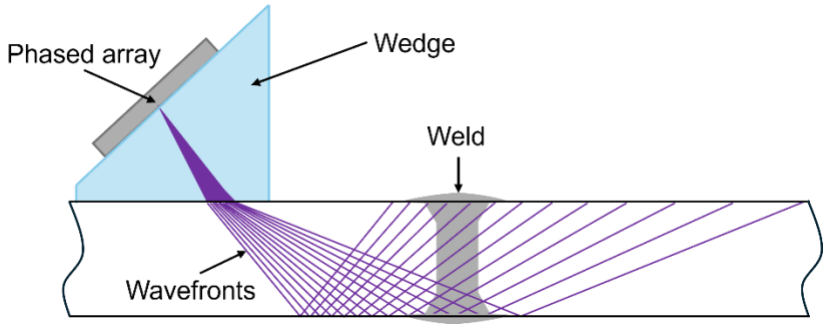

Figure 9. Illustration of phased array ultrasonic testing (PAUT) showing beam steering and focusing capabilities for weld inspection. By electronically controlling the delay patterns across multiple transducer elements, the acoustic beam can be swept through a range of angles and depths to enhance defect detection.

Applications of PAUT for Austenitic Stainless-Steel Inspection

Although the nature of phased arrays makes inspection of austenitic steel welds more feasible, it is not without its challenges. Jiang et al. [26] demonstrated that conventional PAUT imaging may result in localization errors when inspecting such welds. To mitigate this, they implemented the Total Focusing Method (TFM) with a path-corrected model that enabled more accurate calculation of ultrasonic propagation paths in anisotropic media. The approach significantly improved defect localization and image resolution, emphasizing the

importance of accounting for material anisotropy in austenitic weld inspections.

PAUT has also been applied to the inspection of extremely thin steel plates. Naserabadi and Sodagar [27] successfully applied a 5 MHz phased array system to detect both surface and in-depth defects in 0.63 mm thick steel plates using a multi-point focusing technique. Their results showed that PAUT could achieve high spatial resolution and detecting defects as small as 1–2 mm in diameter even in such thin plates.

Several recent studies have further investigated how probe design, wave modelling, and imaging strategies can be optimized for PAUT in austenitic steel, with particular focus on applications relevant to the nuclear industry. Jiang et al. [26] and Connolly et al. [28] emphasized the need for wave path correction and anisotropic modelling to improve defect localization in austenitic welds typical of nuclear piping and pressure vessel components. Dugan and Wagner [29] examined stress corrosion cracks in welds produced to simulate nuclear plant service conditions and demonstrated the difficulties of single-sided inspection under constrained geometries. Kumar et al. [30] showed that dual matrix array probes can significantly enhance signal-to-noise ratios and improve flaw sizing in thick stainless steel welds, particularly relevant to nuclear fabrication. For dissimilar metal welds (DMWs), which are widely used in reactor primary systems, Han et al. [31] demonstrated that geometric-based delay laws and full matrix capture can improve inspection reliability in highly scattering interfaces.

The 2023 Virtual Round Robin study by Virkkunen et al. [32] represents one of the most comprehensive benchmarking efforts for PAUT on DMWs in nuclear settings. Using realistic multi-channel phased array data from water-water energetic reactor steam collector welds, the study revealed considerable variability among human inspectors when interpreting complex ultrasonic datasets, even under standardized procedures. The study also highlighted the potential of machine learning to assist inspectors by ensuring consistent data interpretation and flaw detection, particularly in peripheral channels that are prone to oversight. These findings highlight the potential gain of integrating digital tools and rich datasets to address human limitations in ultrasonic inspection of nuclear welds.

Several promising techniques have been developed to improve the processing and interpretation of PAUT data, especially in complex nuclear applications. One example is the use of advanced image analysis methods based on artificial intelligence (AI), such as so-called convolutional neural networks (CNN) [33]. These models have shown good potential in automatically identifying and highlighting defects in ultrasonic images. Figure 10 from [33] illustrates how different neural network architectures can yield variations in the predicted flaw locations when applied to the same PAUT data, highlighting the influence of the post-processing approach on the final imaging result. These models can reduce interpretation time and improve consistency between inspectors. An Aalto University spin off company called TrueFlaw[1] offers leading AI tools for automatic defect recognition which is highly beneficial when inspecting large areas due to the vast amount of data generated.

Other developments, such as the use of special wave modes (e.g., guided waves) for thin components [27] help adapt PAUT to different inspection scenarios. Techniques like Total Focusing Method (TFM), plane wave imaging (PWI), and synthetic aperture focusing (SAFT) are also increasingly used to enhance image quality, shown in Figure 10. Together, these technologies offer the potential for faster, more accurate, and more reliable inspections of critical components in nuclear environments [33].

One of the key advantages of PAUT is its ability to generate real-time, sectorial scans, which provide a visual representation of the inspected volume [34]. This enables inspectors to evaluate quality and identify potential defects more intuitively than with conventional UT. Additionally, PAUT systems can be programmed to follow predefined scan patterns, making them well-suited for automated or robotic inspection setups. These features are particularly beneficial when inspecting complex geometries or large surfaces with robotics or ROVs. The combined use of robotic inspection with AI-supported tools for defect identification and localization presents a promising way to handle the collection and analysis of high volumes of data. An example workflow suggested by Hu et al. [35] for the automated inspection of steel bridge decks using Deep Convolutional Generative Adversarial Network (DOGAN) for the augmentation of PAUT

[1] https://trueflaw.com

images and You Only Look Once (YOLO) crack identification algorithm, is shown in Figure 11.

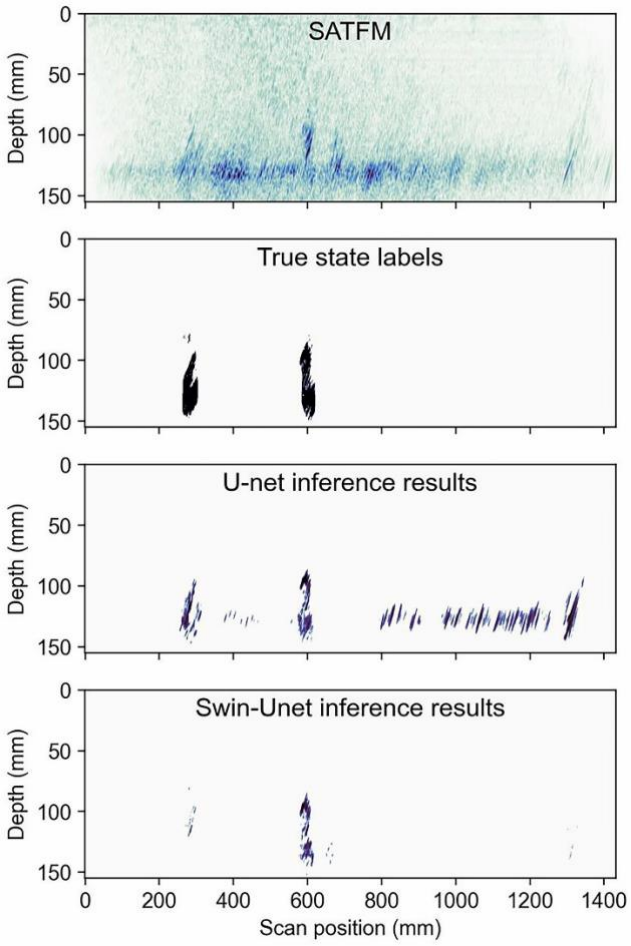

Figure 10. PAUT imaging using combined SAFT and TFM (SATFM). The top plot shows the reconstructed image as viewed by the inspector, while the second plot presents the ground-truth flaw positions. The two lower images show results obtained using two different neural network architectures (U-Net and Swin-U-Net), illustrating differences in predicted flaw locations. Reproduced from Sorger et al. [33], licence under CC BY 4.0.

To enable PAUT in submerged environments such as spent nuclear fuel pools, special consideration must be given to the transducer design and its coupling with water. For automated inspections, it is common to use water feed systems to ensure that the PA probes are properly coupled to the subject under test, which can be seen in Figure 12. However, in fully submerged conditions, such as those found in pool liner inspections, external coupling is no longer required, but the transducers themselves must be specifically

designed to operate underwater. Despite the relevance of this application, little information is available in the literature regarding PAUT systems developed for underwater nuclear inspections. One relevant study by Rodrigues et al. [36] presents a custom-designed 2D phased array transducer capable of volumetric imaging in water, suggesting promising pathways for adapting PAUT to submerged environments.

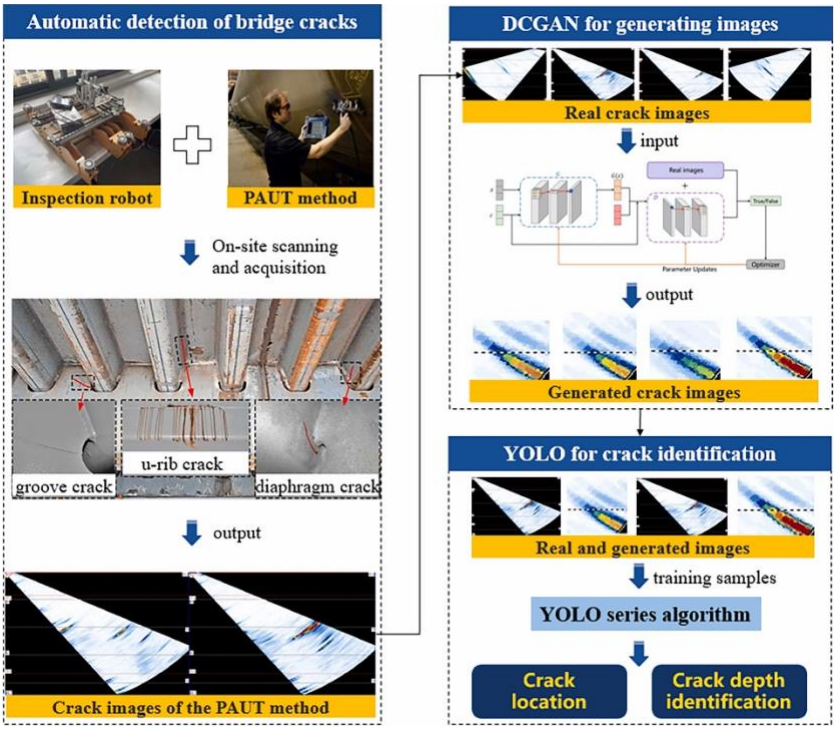

Figure 11. Automated PAUT inspection framework integrating robotic scanning and deep learning-based flaw evaluation as suggested by Zhang et al. [35], licensed under CC BY 4.0.

Despite the progress and flexibility of PAUT in various nuclear applications, its implementation for submerged inspection of thin-walled austenitic stainless-steel pool liners remains an open research area. The specific combination of inspection challenges including complex weld geometries, anisotropic grain structures, and restricted access, requires tailored solutions. While PAUT has shown promising results in both thick and thin sections, as well as in dissimilar welds, there is limited practical experience and published research focused on full in-situ underwater implementation for pool liners.

Figure 12. Scan setup for dissimilar weld mock-up. Adapted from Virkkunen et al. [32]. Observe the water-feed to the transducers to the left in the figure. Licensed under CC BY 4.0.

In particular, the adaptation of water-coupled transducers for robotic or ROV-mounted inspections in radioactive, submerged environments needs further development. Questions also remain regarding the detectability of surface-breaking or through-wall cracks in 3 mm concrete-bonded liners. The current international standard for PAUT of thin-walled steel components, ISO 20601:2018 [37], applies to wall thicknesses ranging from 3.2 mm to 8 mm, and is primarily intended for pipe and flat product inspections under controlled conditions. As such, it does not specifically address the unique challenges associated with submerged, concrete-bonded liners in nuclear pools.

Further experimental validation, the integration of PAUT with robotic or ROV-based inspection platforms, and the implementation of AI-driven defect recognition is needed to fully evaluate the method's capability in nuclear pool liner inspections.

3.1.3 Acoustic Emission

Acoustic emission (AE) refers to the generation of transient elastic waves during the sudden redistribution of stress in a material. This typically occurs when a defect such as a crack initiate or propagates, as illustrated in Figure 13. Unlike conventional ultrasonic testing, which introduces external sound waves into a material, AE is a passive technique that listens for the material’s own response to stress, typically ultrasonic transients. As such, AE is particularly valuable for detecting active damage mechanisms in real time.

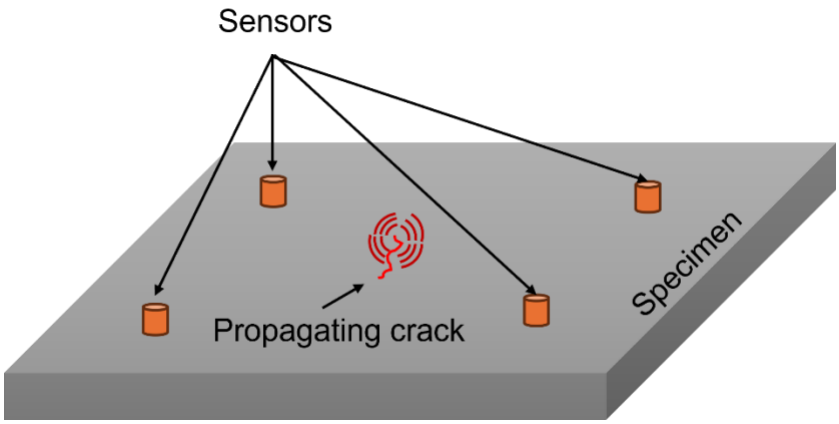

Figure 13. Crack propagation triggers the release of stress waves – acoustic emission.

Sensors are placed on the surface of the material to detect the high-frequency waves emitted by damage events. By analysing the arrival time and characteristics of these signals at multiple sensors, it is possible to estimate the source location and, to some extent, infer the type of defect. AE is highly sensitive to many types of defects, including stress corrosion cracking [38, 39], crevice [40] and pitting corrosion [41], and can detect microcrack activity before it becomes visible or leads to failure. However, successful application requires a source of stress, e.g., thermal, mechanical, or pressure-induced, to activate damage processes. For example, the detection of CO_2 leakage can be achieved by the high frequency sound that is emitted due to the pressurized gas leaking through a small defect [42]. AE has also been successfully applied to locate acoustic emissions during reactor containment pressure tests [43].

AE activity is typically only produced when the previously applied maximum stress level is exceeded, a phenomenon known as the Kaiser effect [44]. However, this effect is valid only up to a certain load threshold. Beyond this point, reapplying a load may trigger AE events (hits) at stress levels lower than the previous maximum. This behavior is referred to as the Felicity effect [44]. These effects are illustrated in Figure 14, where the number of AE hits is plotted against the applied load.

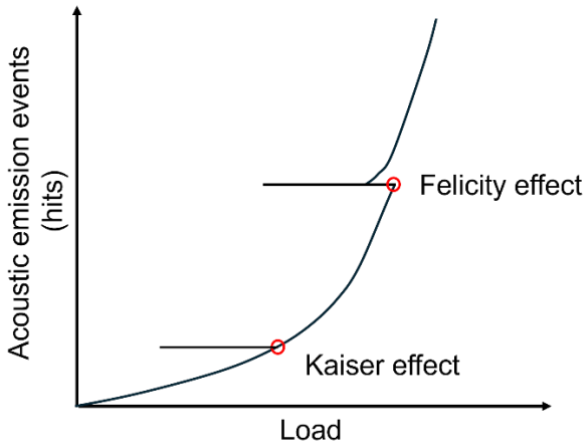

Figure 14. Illustration of the Kaiser and Felicity effects in acoustic emission.

Because AE only responds to active defect growth or, in some cases, pressurized media seeping through tight cracks, it is best suited for monitoring rather than imaging. Although acoustic emission has been used to detect leak-related signals in pressure vessels or systems with high flow velocity, the low-pressure seepage typical of pool liner leakage is unlikely to generate measurable emissions. In this context, AE may serve as an early warning system for crack initiation or leak development, provided that the stress conditions are sufficient to trigger acoustic activity.

Despite its strengths in detecting active damage, AE presents several limitations when applied to leakage localization in pool liners. AE requires a triggering event, such as crack propagation or pressure-driven flow, to generate measurable signals; however, pool liners typically operate under low static stress, and many leakage-relevant defects may be stable and produce no emissions. While AE can in principle be localized using a sufficiently dense sensor network, such arrays would need to be permanently installed, closely spaced, and well-coupled to the liner surface. More importantly, an AE hit does not provide information about defect geometry or leakage relevance, meaning that a separate NDT technique would still be required to identify and characterize the actual flaw. For these reasons, AE is best positioned as a supplementary monitoring tool rather than a standalone method for locating leakage in pool liners.

3.2 ELECTROMAGNETIC WAVE METHODS

When an alternating magnetic field interacts with a conductive material, it induces circulating currents known as eddy currents. These currents generate secondary magnetic fields that oppose the original field, resulting in a characteristic electromagnetic response. The distribution and intensity of these eddy currents are governed by the excitation frequency, the material's electrical conductivity and magnetic permeability, and the geometry of the object under test. Much like how wavelength governs sensitivity in ultrasonic testing, in electromagnetic methods the skin depth, which is the effective penetration of the field, determines which defects can be detected. Higher frequencies provide better resolution but reduce penetration, making them most suitable for surface or near-surface flaw detection.

Electromagnetic testing methods are inherently sensitive to variations in material properties and surface geometry. Changes in conductivity, permeability, or wall thickness caused by defects such as cracks, pitting, or corrosion, alter the local eddy current flow and can therefore be detected. Moreover, these methods are contactless and typically require minimal surface preparation, making them attractive for automated or robotic scanning. However, their application is limited in low-conductivity environments or where deep flaw detection is required.

This report focuses on the following electromagnetic wave-based techniques:

- Eddy Current Testing (ECT) – sensitive to surface and near-surface flaws, commonly used in conductive materials.
- Pulsed Eddy Current (PEC) – uses low-frequency, transient magnetic fields to enable wall-thickness evaluation and subsurface inspection.
- Alternating Current Field Measurement (ACFM) – allows detection and sizing of surface-breaking cracks without the need for direct electrical contact or extensive surface cleaning.

While other electromagnetic techniques exist, such as magnetic flux leakage or remote field eddy current testing, they are primarily intended for ferromagnetic materials or thick-wall inspections and are therefore not emphasized here. The following sections present the state-of-the-art for ECT, PEC, and ACFM, with a focus on weld and

corrosion inspection in stainless steel, and their potential for robotic or underwater deployment in nuclear pool liner environments.

3.2.1 Eddy Current Testing (ECT)

Introduction to ECT

When an alternating electric current is applied to a coil, it produces a time-varying magnetic field. If a conductive material is placed nearby, this magnetic field induces circulating currents within the material, so-called eddy currents. These currents are analogous to swirling eddies in water that form when the flow is disturbed by an obstacle, as illustrated in Figure 15. In materials testing, the presence of cracks [45], corrosion [46], or changes in thickness disrupts the normal flow of eddy currents, leading to measurable changes in the coil's electrical response. By analysing these changes with specialized probes, eddy current testing (ECT) enables the detection of surface and near-surface discontinuities in conductive materials.

The effectiveness of ECT depends on several key parameters, including the excitation frequency, electrical conductivity, and magnetic permeability of the test material. One important concept is that eddy current density decreases exponentially with depth, this phenomenon is known as the *skin effect*. This occurs because the alternating magnetic field induces opposing eddy currents that limit penetration into the material. The *skin depth*, which defines how deeply the currents penetrate, is inversely proportional to the square root of the frequency. Higher excitation frequencies result in shallower penetration, making ECT most effective for detecting surface and near-surface flaws, typically within the first 1–2 mm of depth.

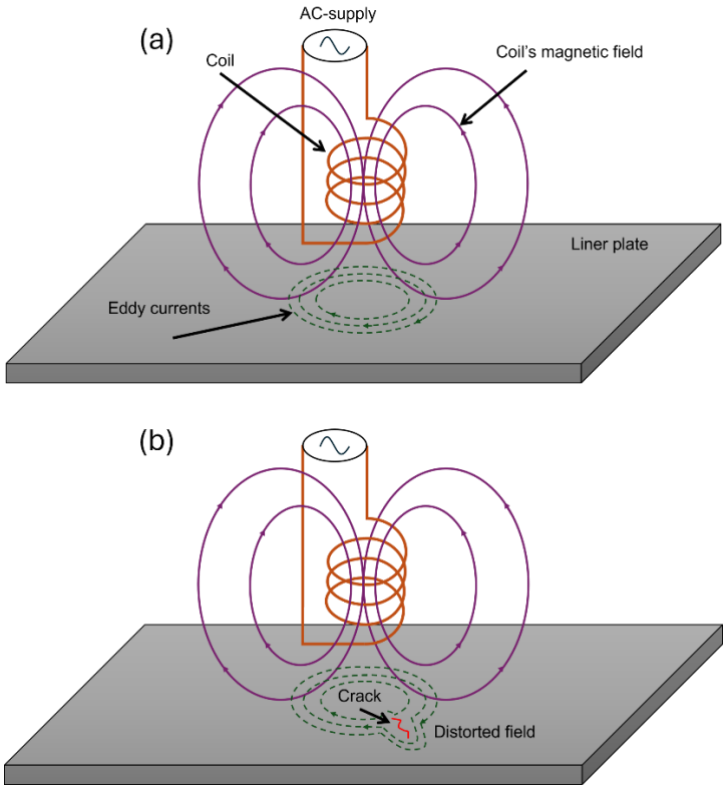

Figure 15. Principle of Eddy Current Testing (ECT). (a) Induction of eddy currents in a defect-free conductive material. (b) Distortion of eddy current flow caused by a surface-breaking crack.

Another critical factor is lift-off, the distance between the probe and the material surface. Even small variations in lift-off caused by surface roughness, coating thickness, or probe wobble can significantly influence signal quality and flaw detectability [47]. Distortion caused by lift-off is showcased in Figure 16, adapted from Xie et al. [48]. It is possible to use model-based inversion techniques [49] or current-

normalized compensation methods that adjust the response signal based on excitation fluctuations [48], as illustrated in Figure 16.

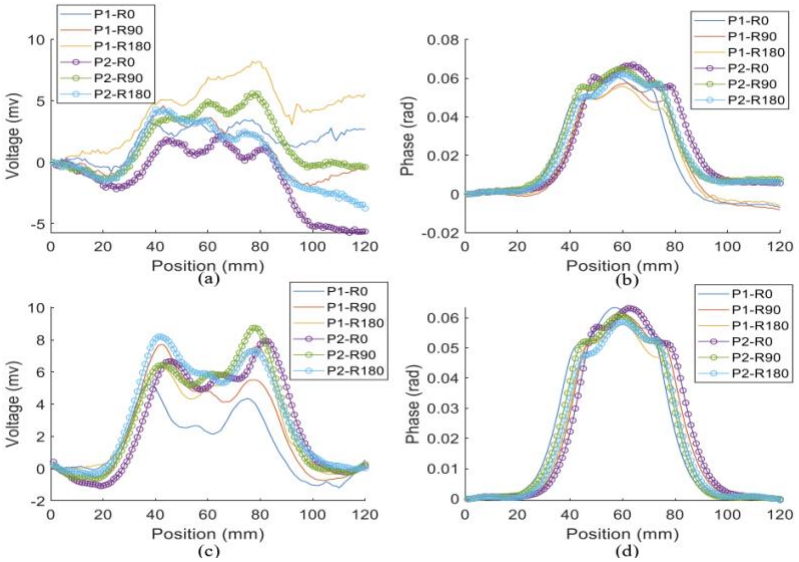

Figure 16. Eddy current response signals showing the effect of lift-off correction. Plots (a) and (b) show voltage and phase before correction; plots (c) and (d) show the corresponding signals after correction using excitation current normalization. Adapted from Xie et al. [48], licensed under CC BY 4.0.

Applications of ECT for Austenitic Stainless-Steel Inspection

The application of ECT to austenitic stainless steel presents additional challenges. Austenitic steel is typically non-magnetic and has relatively high electrical resistivity, which reduces eddy current strength and limits penetration depth. Nonetheless, ECT remains effective for detecting surface-breaking flaws in such materials, particularly at welds and heat-affected zones. In submerged environments, however, ECT performance is further complicated by the conductive nature of water, which can interfere with the magnetic field and increase signal noise.

Despite the challenges, several studies have demonstrated the applicability of ECT for detecting surface and near-surface flaws in austenitic stainless steel, even in complex weld regions. Berkache et al. [50] showed that accounting for localized variations in magnetic permeability, induced by welding in AISI 304, significantly improves the detection of thin circumferential cracks using a stochastic finite element model. Their experimental work on welded pipes

demonstrated that eddy current signals vary strongly with crack depth and probe frequency.

Xie et al. [48] further validated ECT for detecting both surface and sub-surface flaws in 10 mm thick austenitic stainless steel plates through 3D simulation and experimental verification. The study confirmed the effect of scanning direction and the importance of magnetic field component orientation on signal clarity. In addition, Wan et al. [6] demonstrated that plastic deformation in 304 stainless steel introduces significant changes in permeability and coercivity, leading to increased magnetic noise and altered optimal excitation frequencies. These findings highlight the need for frequency tuning and lift-off compensation when inspecting deformed or cold-worked surfaces, which may be relevant for aged pool liners.

Wu et al. [45] introduced a novel probe configuration that enhances penetration depth using phase-shifted excitation coils, enabling the detection of deeper flaws in stainless steel and a potential avenue for improving sensitivity in concrete-bonded liners. In parallel, Niu et al. [51] demonstrated the integration of eddy current data with convolutional neural networks (CNNs) for automated flaw classification in welded 304L stainless steel plates. Their approach converted raw scan data into image representations of real and imaginary signal components, achieving reliable crack identification in a proof-of-concept test. While demonstrated on idealized defects, the study highlights the potential for combining ECT with AI to reduce operator dependency and support automated inspection workflows. These capabilities are especially relevant for remote or submerged nuclear applications.

Jacob et al. [52] demonstrated the use of a Pulsed Eddy Current (PEC) system mounted on an ROV for underwater thickness measurements of steel structures. The system operated without surface preparation and was effective through marine growth, highlighting PEC's robustness in harsh environments. While the application was focused on offshore structures, the study illustrates the potential of integrating PEC with ROVs for remote inspection in submerged conditions. This approach may be adapted for nuclear pool liners.

Collectively, these studies highlight the feasibility of ECT in detecting relevant defects in stainless steel under various structural and

magnetic conditions, even under water. However, their application to thin, submerged, and concrete-bonded pool liners remains largely unexplored. To make ECT and PEC relevant for the current context, continued development of probe designs, signal correction algorithms, and simulation-informed inspection strategies tailored to the constraints of nuclear power plant environments is required.

3.2.2 Alternating Current Field Measurement (ACFM)

Introduction to ACFM

Alternating Current Field Measurement (ACFM) is an electromagnetic NDT technique that enables the detection and sizing of surface-breaking defects in metallic structures. Unlike eddy current testing (ECT), ACFM uses a uniform alternating magnetic field generated by an excitation coil inside the probe. This alternating field induces a controlled surface current in the material beneath the probe, even under water. When a surface-breaking crack is present, the flow of this induced current is perturbed, generating distinctive changes in the local magnetic field. These perturbations are measured using orthogonally placed magnetic sensors, typically referred to as the *Bx* and *Bz* channels. The Bx signal primarily relates to crack depth and exhibits a trough due to reduced surface current density above the defect. The Bz signal responds to the redirection of current around the crack tips. A clockwise or counterclockwise deflection results in characteristic peaks and troughs. The separation between these peaks is used to estimate the crack length [53]. The principle of ACFM is illustrated in Figure 17.

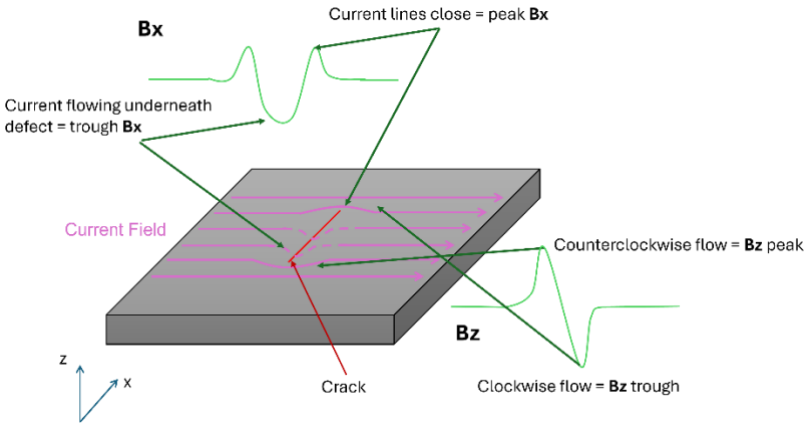

Figure 17. Principle of Alternating Current Field Measurement (ACFM). A surface-breaking crack disturbs the surface current, resulting in characteristic changes in the measured Bx (depth-related) and Bz (length-related) magnetic field components above the surface.

A key benefit of ACFM is its low sensitivity to variations in lift-off and coating thickness, allowing reliable inspection even through non-conductive coatings up to several millimeters thick [53]. This makes it highly suitable for field applications where surface preparation is limited, or underwater deployment is required. Additionally, the technique is capable of quantifying defect geometry without the need for calibration on known flaw sizes, offering a faster and more operator-independent alternative to traditional methods like Magnetic Particle Inspection or Penetrant Testing [54].

Applications of ACFM for Austenitic Stainless-Steel Inspection

In the context of stainless-steel pool liners in nuclear power plants, ACFM has shown strong promise. Wei et al. [55] applied ACFM to inspect welds in 3 mm thick austenitic stainless steel panels from spent fuel pools and demonstrated a detection threshold for surface cracks as small as 2 mm in length. A 3-axis probe and automatic scanning equipment enabled the inspection of complex geometries, including weld toes and heat-affected zones.

Shen et al. [56] investigated ACFM's sizing performance for angled cracks, highlighting how crack orientation affects the Bx and Bz signals. Their results show the importance of probe alignment and signal interpretation when dealing with non-vertical defects, a realistic challenge in welds and pool liners.

Several developments have specifically targeted underwater nuclear environments. A European inspection campaign, carried out with

support from Cete Apave and TSC Inspection Systems, adapted ACFM for robotic deployment in spent fuel pools. The probe was designed to navigate tight spaces under fuel racks (clearance of only 35 mm) and was successfully mounted on both vertical wall crawlers and bottom-surface ROVs [53]. The system detected through-wall defects greater than 5 mm and performed reliably in radiation doses up to 600 Gy [53].

Additionally, Qi et al. [57] investigated ACFM for the inspection of flat butt welds in 4 mm thick 304L liners using artificial surface-breaking defects, including cracks with lengths of 6, 3, and 2 mm (all with 0.3 mm opening) as well as flat-bottom holes with diameters of 1.0, 0.5, and 0.3 mm. They concluded that ACFM was able to detect all investigated defects, whereas Eddy Current Array failed to detect several of them.

Furthermore, a field study reported by Yuan et al. [58] reports reliable detection of 3 mm long through-wall cracks in austenitic stainless steel liners using ACFM deployed on an underwater robotic platform in an operating nuclear facility. This study illustrates that ACFM can achieve high sensitivity also under realistic underwater inspection conditions when combined with appropriate probe design and deployment strategies.

Laboratory and underwater trials demonstrated strong agreement between simulation and experiment, validating finite element models of crack interaction with the magnetic field [59, 60]. Furthermore, the inspection process was compatible with diver-assisted and robotic deployment, and real-time visualizations aided in probe positioning and defect recognition [53].

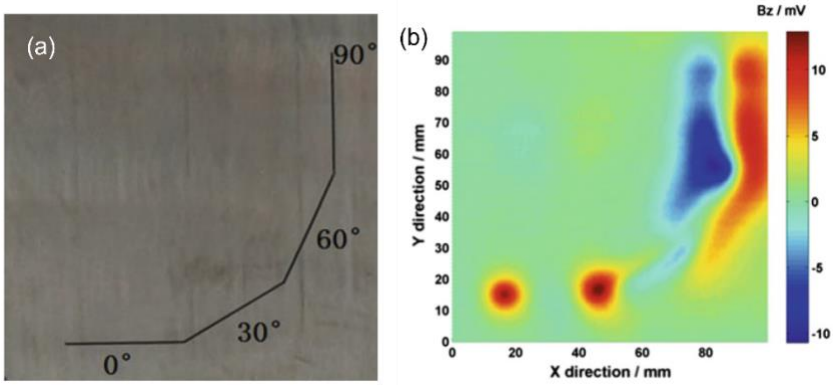

Figure 18. Visualization of irregular crack in austenitic stainless steel using ACFM. Adapted from Yuan X. et al. [61], licensed under CC BY 4.0.

Despite its strengths, ACFM is not without limitations. Sensitivity to shallow flaws diminishes with increased lift-off or surface coating thickness. The probe size and scanning speed must be tailored to the application, and while ACFM provides good geometric estimates of crack size, it does not offer volumetric imaging like PAUT. In addition, as with other electromagnetic methods, ferromagnetic inclusions in the concrete backing (e.g., magnetite aggregates) may introduce local field distortions that need to be considered in inspection planning.

Collectively, these studies strongly support the suitability of ACFM for the inspection of nuclear pool liners. Its resilience to coating, low lift-off sensitivity, lack of need to calibrate against known defects, and the compatibility with robotic deployment make it an attractive option for remote in-situ inspection of nuclear pool liners.

3.3 OPTICAL METHODS

3.3.1 Visual Testing and Photogrammetry

One of the ways to currently inspect the liners is to visually examine them after draining and sanitizing. Visual testing can be done in connection with penetrant testing, a method in which a fluorescent fluid is applied to an area and then wiped off to highlight surface-breaking defects. As stated, this requires drainage and sanitation of the pools before personnel can perform the inspection. Fortunately, there have recently been rapid developments in the field of drone-based photogrammetry which can render very high-resolution images of otherwise hard-to-reach elements. This facilitates a 3D

reconstruction of the structure and along with machine learning and other AI-tools it is possible to characterize defects such as cracks with high precision [62]. An example is shown in Figure 19 where crack mapping on a concrete surface using technology from Spotscale is shown.

Figure 19. AI-supported high-resolution photogrammetry using drones for remote crack mapping on concrete surfaces. Cracks are highlighted in yellow. Figure from Spotscale.

Several recent studies have demonstrated the viability of photogrammetry-based crack detection in submerged or low-visibility conditions. Li et al. [63] introduced an enhanced underwater crack detection pipeline combining image enhancement, adaptive thresholding, and deep learning. Their system was validated on low-contrast underwater footage and showed high detection accuracy for thin and irregular crack patterns, even under dynamic lighting and turbidity. Chen et al. [64] further highlighted that photogrammetry, when fused with AI-based post-processing and visual SLAM (Simultaneous Localization and Mapping), enables scalable defect detection on complex surfaces such as pipelines, concrete walls, and steel structures.

These findings point to the potential for integrating photogrammetric inspection with robotic platforms in nuclear pool environments, offering a non-contact and scalable solution for identifying visual indicators of leakage, corrosion, or liner damage. While these systems currently focus on surface-visible features, their high resolution and adaptability make them well-suited to complement NDT techniques

by providing context, aiding localization, and enabling long-term intuitive inspection.

3.4 SYNTHESIS OF LOCALIZATION METHODS

This report has reviewed and evaluated a range of non-destructive testing (NDT) techniques for locating leakage or leakage-prone defects in stainless steel pool liners used in nuclear power plants. These techniques fall broadly into three categories: mechanical wave-based methods, electromagnetic methods, and visual/optical approaches. Each class offers unique strengths and limitations depending on defect type, accessibility, material properties, and environmental constraints.

Mechanical wave methods, particularly Phased Array Ultrasonic Testing (PAUT) and Shear-Horizontal (SH) guided wave EMATs, provide robust options for detecting and characterizing surface-breaking and through-wall cracks. EMAT-based guided wave techniques are attractive for austenitic steel inspection due to their ability to operate without fluid couplants and their potential for integration with robotic platforms. However, material anisotropy, grain scattering, and mode complexity limit achievable resolution, particularly for very small defects. Guided wave approaches offer long-range coverage but are generally better suited for screening than for precise localization. Acoustic Emission remains a capable monitoring technique for damage initiation and growth, but it is not considered suitable for leakage localization due to the low acoustic activity expected from small, steady leaks.

Electromagnetic techniques, including Eddy Current Testing (ECT) and Alternating Current Field Measurement (ACFM), are highly sensitive to leakage-relevant flaws and can operate through coatings. While ECT is generally more established, ACFM's stability at higher lift-off and crack-sizing capabilities make it particularly suited for robotic applications. Both techniques are constrained by penetration depth and conductivity-related signal strength in austenitic stainless steel, but recent developments in probe design and signal correction have shown promise. Underwater deployment is feasible and demonstrated, especially in the context of robotic or ROV-based platforms.

Remote visual testing and photogrammetry, while limited to surface-visible features, offer scalable, non-intrusive inspection options that

are well suited for mapping and contextualizing defects. When paired with machine learning approaches, such methods can assist in identifying areas of interest and guiding the application of more advanced NDT techniques, rather than serving as standalone localization tools.

3.4.1 Multimodal Fusion and Future Directions

A key insight from this review is that while several NDT methods show strong potential for leakage localization in stainless-steel pool liners, each technique addresses different aspects of the inspection challenge. No single method can fully satisfy all requirements imposed by submerged operation, limited access, and the need to detect small, leakage-relevant defects. Consequently, a multimodal inspection approach, in which complementary methods are combined, offers a robust path forward.

In such an approach, surface-sensitive electromagnetic techniques such as ACFM can serve as the primary tool for detecting and localizing leakage-relevant surface-breaking cracks, while ultrasonic methods such as PAUT provide complementary information for defect characterization and weld interrogation where required. Visual inspection and photogrammetry can be used to rapidly map surfaces, document features, and guide the placement of more advanced NDT probes. SH-wave EMAT techniques may further contribute as couplant-free screening tools in selected scenarios but are best regarded as complementary rather than standalone localization methods.

In addition, Acoustic Emission (AE) monitoring can provide valuable contextual information in a multimodal inspection framework. While AE is not well suited for precise localization of established leaks in pool liners, sustained or intermittent AE activity may indicate regions of ongoing damage evolution or material degradation. Such information can be used to prioritize inspection areas and guide the deployment of targeted methods such as ACFM and PAUT, thereby improving inspection efficiency and focusing resources where they are most likely to be needed.

The integration of these modalities can be further enhanced through digital workflows, where visual data support registration and navigation, and signal-based measurements provide quantitative defect information. AI-assisted image analysis and decision-support

tools may help prioritize inspection zones and manage large data volumes, while digital twin concepts offer a longer-term framework for integrating inspection results over time. Although such integration remains technically demanding, ongoing advances in sensor miniaturization, robotic deployment, and data fusion are steadily improving feasibility.

Continued development of multimodal inspection concepts is therefore essential to achieving reliable, in-situ, and cost-efficient leakage localization in stainless-steel pool liners, particularly in submerged and access-limited nuclear environments.

4 Robotic Deployment

Non-destructive testing methods suitable for locating leakage in pool liners must ultimately be compatible with remote deployment in submerged, and potentially radioactive environments. Since draining and sanitizing spent fuel or condensation pools is a resource-intensive and hazardous process, there is strong incentive to conduct inspections in-situ. This necessitates the use of remotely operated vehicles (ROVs) or other robotic manipulators capable of delivering sensors and probes with sufficient precision, stability, and repeatability.

ROVs are already widely used across the nuclear and offshore sectors for visual inspection and environmental monitoring. However, adapting them for contact-based or near-contact NDT methods, such as PAUT, EMAT, ECT, or ACFM, introduces new technical challenges. These include ensuring proper probe orientation and positioning, maintaining stable lift-off or contact pressure, and navigating within confined spaces or complex geometries.

Different classes of manipulators may be considered depending on the inspection scenario. Free-floating ROVs offer mobility and are well suited for carrying imaging systems or non-contact sensors. Crawler-based systems, often using magnetic or suction adhesion, can be used for wall-following tasks and provide better positional stability during scanning and for contact sensors. More advanced systems may incorporate robotic arms or articulated probe mounts, enabling controlled scanning motions and consistent coupling on curved or vertical surfaces. Fortunately, several commercial manipulators exist. The following section will present a selection of robotic platforms and technologies that can be of interest to consider for underwater applications.

4.1 ROBOTIC PLATFORMS FOR UNDERWATER NDT

To enable in-situ non-destructive testing of submerged pool liners, manipulators must support precise positioning, reliable navigation, and integration with various NDT probes. Several commercial platforms have demonstrated capabilities relevant to the inspection of pool liners in nuclear power plants. These platforms range from compact ROVs suitable for visual inspection to advanced crawlers

capable of delivering ultrasonic or electromagnetic probes with high spatial accuracy.

Framatome offers a remotely operated system known as SUSI (Submarine System for Inspections), developed specifically for inspections inside reactor pools and other confined, submerged nuclear environments. The SUSI (shown in Figure 20) is a neutrally buoyant, free-swimming vehicle that can be maneuvered close to walls and surfaces using a tether and guide system. In addition to visual inspection, SUSI can carry ultrasonic testing equipment, which in current applications is used for inspecting thick components such as reactor pressure vessel core barrel and core baffle bolts [65]. The system has been successfully deployed in European nuclear power plants for detecting indications such as cracks, corrosion, and liner detachment [65].

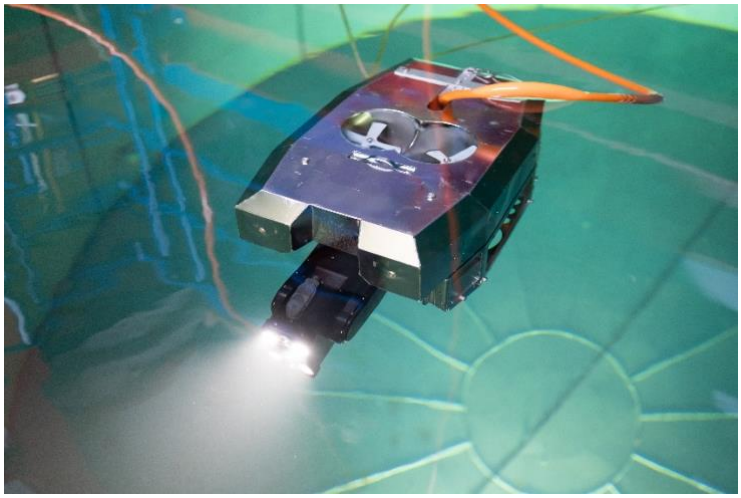

Figure 20. SUSI Gen 3 © Framatome.

While SUSI demonstrates that underwater robotic access is feasible, it is not a turn-key solution for leakage localization in thin stainless-steel liners. The system is not equipped with NDT modalities suitable for detecting small surface-breaking cracks in 3–4 mm austenitic steel, such as ACFM and/or PAUT adapted for thin plates. Furthermore, accurate crack detection in thin liners requires precise probe contact, lift-off control, and high spatial resolution, capabilities that are not part of SUSI's standard toolset. Thus, SUSI should be regarded as a potential carrier platform for future NDT integration rather than an existing solution to the leakage-localization problem.

TSC Subsea is a specialized provider of advanced non-destructive testing systems for subsea and confined-space environments. Their portfolio includes ROV-deployable tools for ultrasonic testing, ACFM, eddy current (ECT), and pulsed eddy current (PEC), all designed for integration with robotic platforms. Notably, TSC Subsea offers modular solutions that allow deployment in complex underwater geometries using multi-axis robotic arms. Their technologies have been successfully used for the inspection of welds, corrosion, and fatigue cracking in hard-to-reach subsea structures, which presents clear parallels to the challenges encountered in nuclear pool liner inspection [66]. An image showing the NodeScanner™ performing ACFM weld inspection can be viewed in Figure 21.

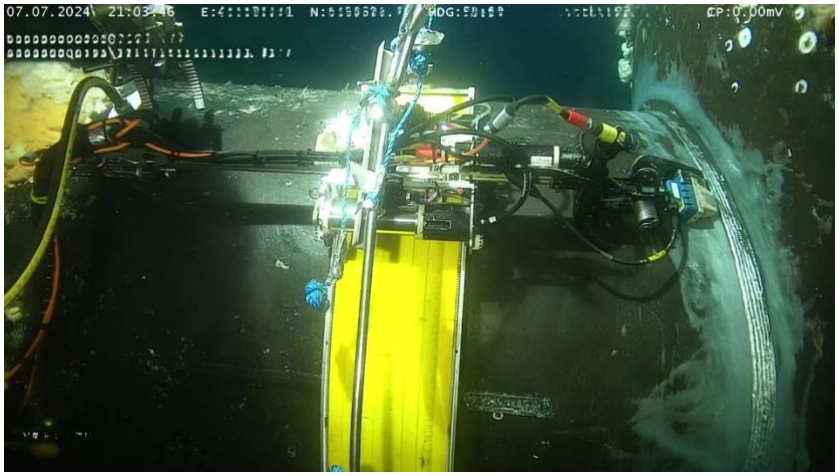

Figure 21. NodeScanner™ performing ACFM weld inspection © TSC Subsea. The ACFM probe can be seen to the right in the figure, near the weld.

Since magnetic-based crawlers cannot be reliably employed on stainless steel, alternatives must be considered. HausBots [67] offer crawlers with the *Aerogrip* technology that facilitates adhesion even on uneven surfaces. This is achieved by using high-volume airflow to create areas with low pressure, thus generating adhesion. HausBots platforms have been applied on a range of different inspection tasks, including conducting UT inside a large stainless-steel tank (see Figure 22). While the current platforms from HausBots are not directly designed for submersible use, the core operating principle is technically feasible for underwater applications.

Figure 22. HausBots HB2 deploying UT probe inside a stainless-steel tank. Image courtesy of HausBots Ltd.

In addition to these integrated NDT solutions, there are several commercially available ROV platforms that offer a high degree of modularity and customization. Systems from Deep Trekker [68], VideoRay [69], and Blue Robotics [70] are commonly used for underwater inspection tasks and can be adapted to carry NDT payloads. While not purpose-built for NDT, these vehicles provide a flexible platform for experimental deployments or integration of custom inspection tools.

Given this brief overview, there is an expanding market of robotic platforms with a varying degree of modularity. These platforms offer a wide range of possibilities for the deployment of relevant NDT modalities. However, it appears unlikely that a turn-key solution exists for the current challenge. While systems such as SUSI and NodeScanner are already deployed for underwater inspection tasks, they are either not equipped with the NDT methods required to detect small surface-breaking defects in thin stainless-steel liners, or in the case of platforms that do carry, for example, ACFM and PAUT, the tools have not yet been adapted, qualified, or demonstrated for this specific application. In addition, current systems do not offer the precise probe contact, lift-off control, and positional accuracy needed for high-resolution inspection of thin liners. The next step, after selecting suitable testing modalities, is therefore to adapt and integrate these techniques for robotic deployment. The challenge lies in keeping the measurement systems and manipulators sufficiently

small and stable to navigate and perform NDT in the restricted access areas of the pools.

5 Experiments with SH-wave EMATs

5.1 SYSTEM CHARACTERIZATION AND CALIBRATION

As identified in Chapter 3.1.1 – Shear-Horizontal (SH) wave generation using Electromagnetic Acoustic Transducers (EMATs) may be suitable for underwater inspection of austenitic pool liners. However, certain aspects need to be investigated, such as the effect of concrete backing, i.e., energy leakage and mode suppression, and the methods capability of detecting small through-wall defects.

To evaluate the feasibility of EMAT-based SH-wave inspection in this context, three key factors must be addressed: impedance matching the measurement system, which governs the efficiency of wave transmission from the transducer into the liner; attenuation, which determines how rapidly the signal decays as it propagates; and shear velocity, which provides the necessary material property input for signal interpretation and defect localization. The following sections examine each of these aspects in detail.

5.1.1 Probes and Measurement System

The experimental setup consists of commercially available EMAT probes in combination with a dedicated high-power ultrasonic measurement system. The main components are described below.

A pair of shear-horizontal EMATs (model SH(G/D)0620S, SONEMAT, UK) centered at 600 kHz (~5 mm wavelength) were procured for these experiments, as shown in Figure 23. The probes have dimensions of 40 × 30 × 20 mm. In the model designation, *G* and *D* denote the Generator (transmitter) and Detector (receiver), respectively.

Figure 23. SONEMAT 600 kHz SH-wave probes.

Because EMATs generally require relatively high drive power to achieve an adequate signal-to-noise ratio (SNR), the transducers were driven using a RITEC RAM-5000 SNAP-Plus system. This unit provides high-power pulse generation (up to 5 kW into 50 Ω) as well as signal reception and digitization. The complete measurement chain is illustrated in Figure 24. To optimize performance, several inline components were included: a high-power 50 Ω termination (RITEC RT50), an EMAT transmit matching network (RITEC TEM), and a preamplifier (RITEC PAS, not shown in the figure).

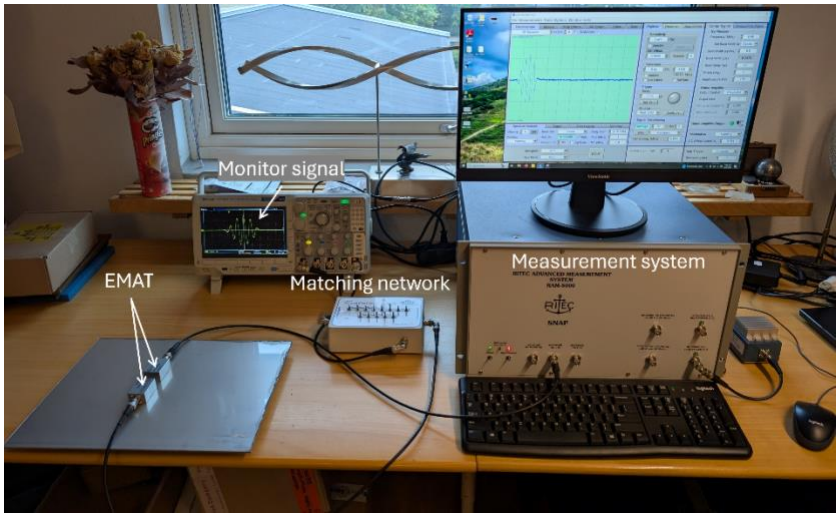

Figure 24. Measurement System for EMAT experiments.

This measurement chain provides the basis for the subsequent investigations into impedance matching, attenuation, and shear

velocity estimation. The sample used for the investigation is a 290 x 390 x 3 mm EN 1.4307 (SS2352/304L) stainless steel plate.

5.1.2 EMAT Impedance Matching

EMATs present an inductive load when driven electrically. If this inductive behavior is not compensated, much of the power delivered from the driver is reflected or stored as reactive energy rather than being converted into useful ultrasonic excitation. The driver for these experiments is a RITEC RAM-5000 SNAP-Plus which is designed to deliver high power pulses into a 50 Ω load. Impedance matching is therefore required to bring the EMAT's complex impedance closer to this reference.

A practical approach is to introduce a series capacitor, which cancels part of the EMAT's inductive reactance at the operating frequency. This reduces the overall mismatch and increases the effective current driven through the EMAT. The matching network (RITEC TEM) is depicted in Figure 25 with a 6.8 nF capacitor switched in.

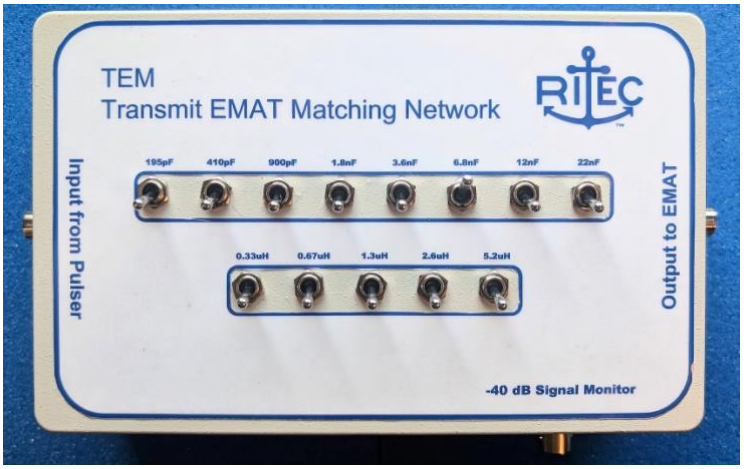

Figure 25. RITEC Transmit EMAT Matching Network.

The TEM enables the monitoring of the signal fed to the transmitting EMAT at a -40 dB level (1/100). With the signal monitor, it is possible to illustrate the effect of matching. Figure 26 shows that without any matching network (blue curve), the drive signal shows reduced amplitude (4.1 $V_{peak\text{-}to\text{-}peak}$) and clear distortion at the end of the burst. When a 6.8 nF capacitor is switched into the circuit (orange curve), the drive amplitude increases (4.4 $V_{peak\text{-}to\text{-}peak}$), and the distortion is eliminated. This indicates more efficient power transfer from the

driver into the EMAT and a cleaner ultrasonic excitation. This setup was deemed optimal as it resulted in the greatest output with minimal ringing.

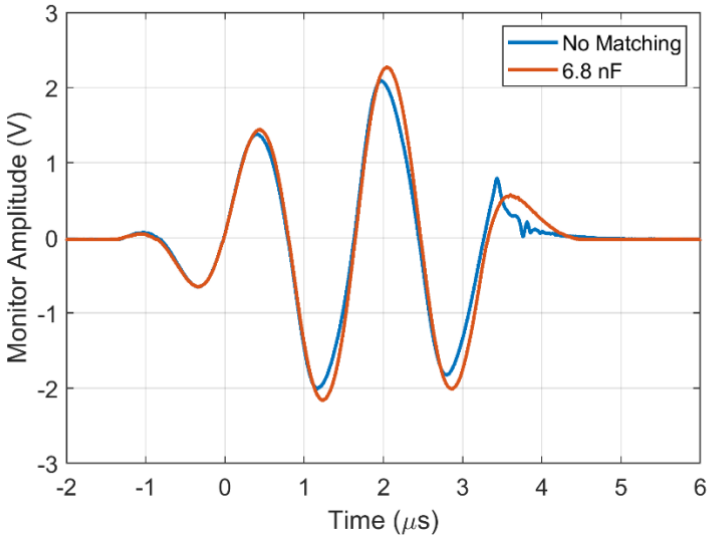

Figure 26. Monitor signals from the EMAT Matching Network with no matching (blue) and 6.8 nF capacitance (orange). Signals are -40 dB with reference to the driving signal.

5.1.3 Attenuation and Shear Velocity Estimation

While it is not expected that stainless steel exhibit very strong acoustic attenuation, it is generally good practice to evaluate attenuation per unit length to better understand the data from inspections. It is also a metric to use when comparing free plate measurements with the bonded plate case.

To understand the material attenuation, it is necessary to make multiple measurements of the signal amplitude at increasing distances between the probes. By plotting the amplitude as a function of distance, and since the system attenuation is kept constant, the material attenuation would be given by the slope of the resulting curve:

$$\boldsymbol{A(d) = A_0 - \alpha \cdot d} \tag{2}$$

where $A(d)$ is the received amplitude in dB at distance d, A_0 is given by all fixed losses (intercept in the curve), and α is the attenuation coefficient in dB per unit length.

The excitation waveform was a Hanning-windowed sinusoidal tone burst with 3 cycles with an amplitude of 440 $V_{peak\text{-}to\text{-}peak}$. Two stages of pre-amplification were used: 20 dB from the PAS and 52 dB from the digitizer in the RITEC SNAP. To improve SNR, the measurements were stacked with 1024 averages. Measurements were made with an initial distance between the probes of 50 mm. The distance increased up to 100 mm with increments of 1 mm. This means that a total of 51 traces were collected.

The first and last trace can be viewed in Figure 27. The raw signals received contained significant electromagnetic (EM) crosstalk which contaminated the signal's early part. The main perturbation appears to be low frequency, which is why the signals were bandpass filtered using a 4th order Butterworth filter with a pass band of 420 – 780 kHz. The filter is shown in Figure 28. This reduced greatly EM crosstalk and the high-frequency noise, resulting in clear signals for further analysis.

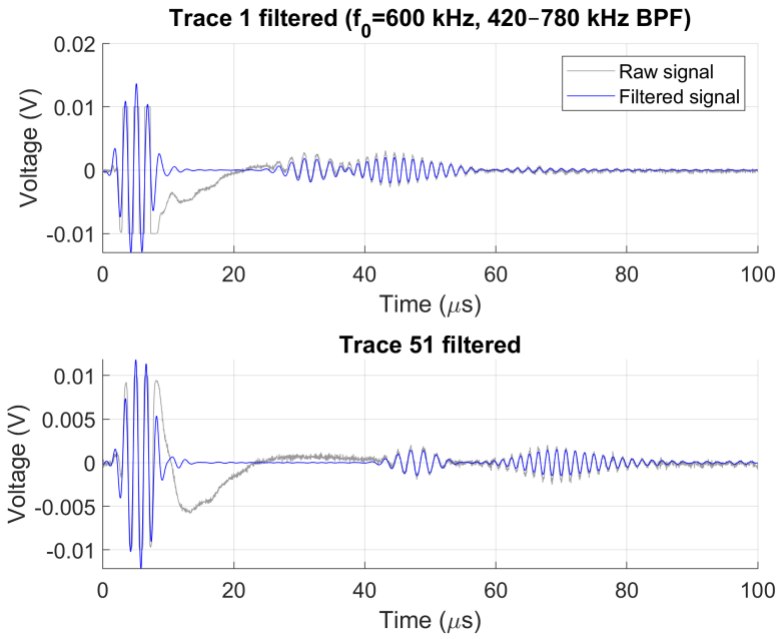

Figure 27. Received EMAT signals at 50 mm (upper plot) and 100 mm (lower plot). The grey curves are the raw signals, and the blue curve are the bandpass filtered signals.

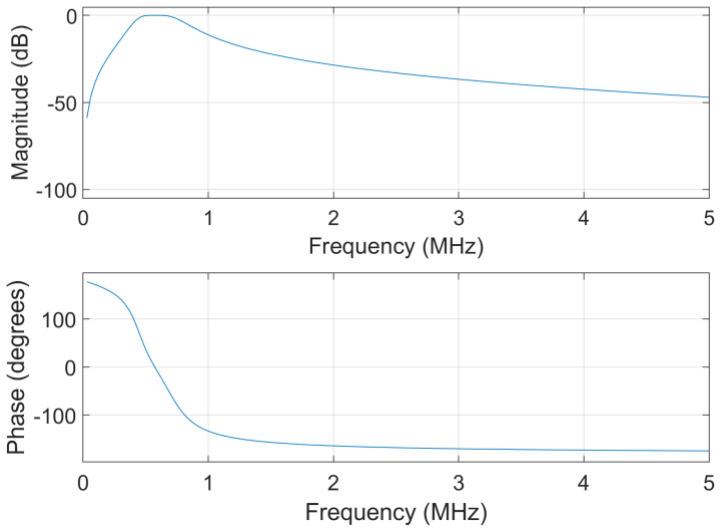

Figure 28. 4th order Butterworth bandpass filter used to improve the clarity of EMAT signals. Passband 420 – 780 kHz.

Figure 29 shows all 51 traces acquired for transmitter-receiver (Tx-Rx) separations between 50 and 100 mm. The first wave packet after the electromagnetic crosstalk (highlighted) is used in the subsequent analysis. A second packet follows shortly thereafter with a clearly different slope of arrival time versus distance, indicating a lower group velocity. This behaviour is consistent with coexistence of the non-dispersive SH0 mode (first arrival) and the dispersive SH1 mode (second arrival). At the chosen frequency, SH1 is supported and travels slower than SH0. Lowering the centre frequency would reduce SH1 content but also increase the wavelength and thus reduce the spatial resolution of the scans.

Shear-wave velocity and attenuation were estimated from the first arrival only. After band-pass filtering and gating, the analytic-signal envelope was computed. For velocity, the time of the envelope peak was paired with the Tx–Rx separation; for attenuation, the gated RMS amplitude was regressed against separation.

Figure 30 plots peak-envelope time versus separation. A linear fit ($t = t_0 + x/v$) yields $t_0 = 15.43\,\mu s$, representing fixed system delays (trigger-to-transmission and peak-picking bias), and $v = 3.067\,mm/\mu s$ (3067 m/s) with $R^2 = 0.9965$. The intercept can be used to time-align the records for visualization and the slope provides the shear-

wave speed used in the subsequent analysis.

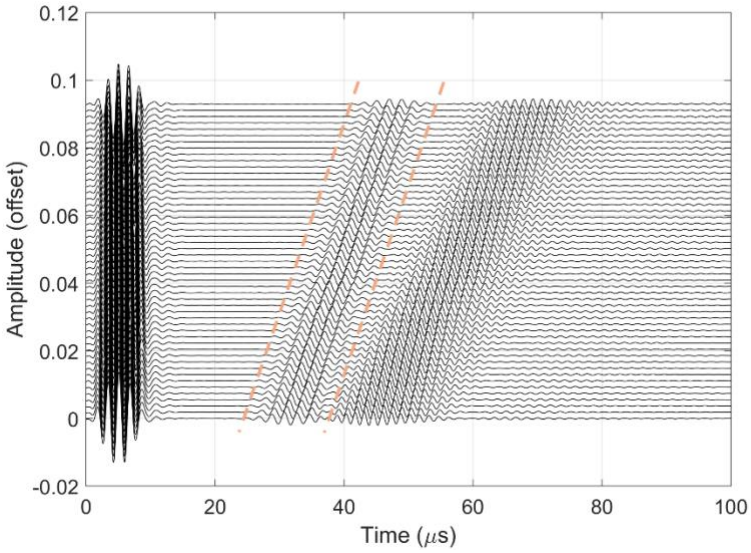

Figure 29. All 51 traces stacked to illustrate a weak drift in arrival time. The bottom trace is for the distance 50 mm, and top is 100 mm. Orange dashed lines highlight the first arrival used for subsequent analysis.

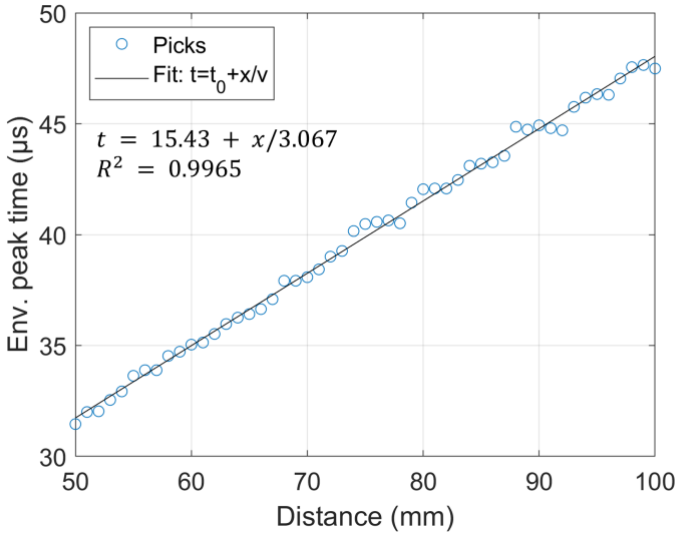

Figure 30. Velocity estimation by peak envelope detection. The estimated shear velocity (3067 m/s) is given by the slope of the line fitted to the time of the peak amplitude for each probing distance.

Using tabulated values for the shear modulus ($G = 74 - 80\ GPa$) and density ($\rho = 7800 - 8000\ kg/m^3$) [71, 72] the expected range of bulk shear velocity can be estimated to be: $c_s = \sqrt{(G/\rho)} \approx 3040 -$

3200 m/s. The determined velocity of 3067 m/s therefore agrees well with the expected values.

As the traces in Figure 29 exhibit a second wave packet, it is wise to examine the analytic group velocity curves for plate SH modes to confirm the presence of the SH1 mode. The group velocity is the speed at which the envelope, thus energy and information, of a narrow-band wave packet propagates. For an isotropic plate of thickness d with traction-free surfaces, the group velocity of the n:th SH mode is given by Eq. (3) [18, 73]:

$$c_{g,n} = c_s \sqrt{1 - \left(\frac{n}{2}\right)^2 / \left(\frac{fd}{v_s}\right)^2} \tag{3}$$

where $v_{g,n}$ is the group velocity for the guided wave mode $n = 0, 1$ for this case, c_s is the bulk shear velocity as determined, and fd is the frequency-thickness product using $d = 3$ mm as the thickness.

The analytical group velocity for SH0 and SH1 with frequencies ranging from 0 to 2 MHz is shown in Figure 31. The dashed line in the figure represents the frequency-thickness product at the excitation frequency for the current experiment (600 kHz), which is clearly above the cutoff for SH1. The influence of SH1 could be reduced by reducing the probing frequency, however, that would also negatively affect the spatial resolution. For 600 kHz, the probing wavelength for SH0 is ~5 mm.

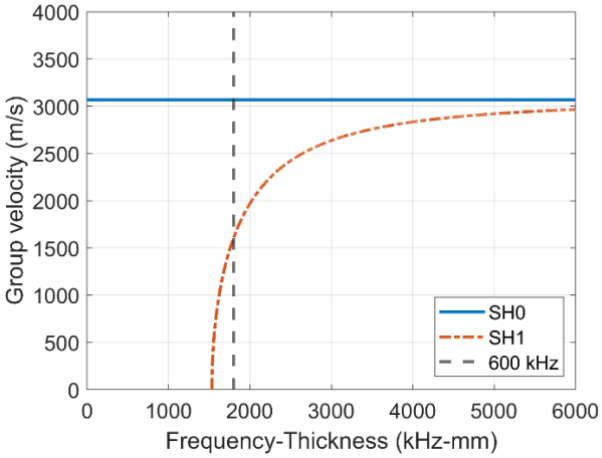

Figure 31. Analytic group velocity curves for the non-dispersive symmetric SH0 mode (blue) and the first dispersive and anti-symmetric mode SH1 (orange dash dotted). Vertical dashed line indicates the frequency-thickness product at 600 kHz and 3 mm.

Attenuation per unit distance was estimated analogously to the velocity analysis but using the RMS envelope amplitude of the first arrival within a fixed gate. The amplitudes (in dB, referenced to the median trace) were regressed against the Tx–Rx separation using Eq. (2). The extracted magnitudes are plotted against the probe separation in Figure 32 along with a curve fitted to the data using. The attenuation is expectedly shown to be low at 0.039 dB/mm with $R^2 = 0.88$, which corresponds to about 3 dB (halved amplitude) over 77 mm. The scatter can be explained by inconsistent placement of the probes as they were moved manually.

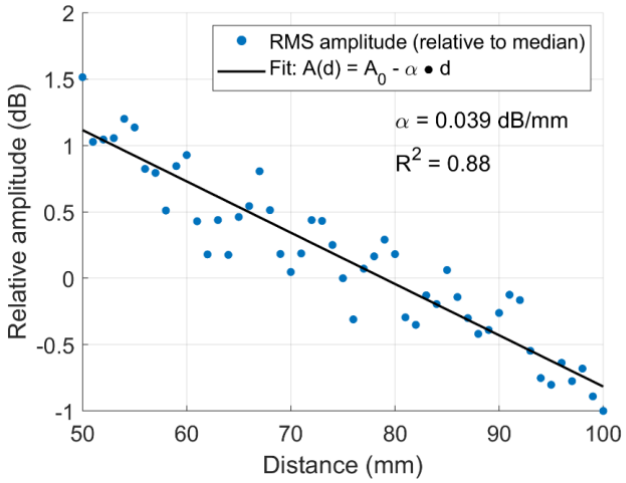

Figure 32. Relative RMS amplitude plotted against distance between probes. The slope of the fitted curve yields an estimate of the attenuation per unit length see eq. (2).

In summary, the baseline measurements confirm that the first arrival is the non-dispersive SH_0 mode with a shear-wave speed of 3067 m/s and wavelength ≈ 5 mm at 600 kHz, while a slower SH_1 packet is present as predicted by dispersion theory. The path-dependent amplitude decay is modest (α = 0.039 dB/mm), which is compatible with the planned probe separations. These results establish the operating point and provide calibration constants (t_0, v_s) that can be used to time-align traces. In the next section, this calibration is applied in one-dimensional line scans over a plate with machined defects and construct transmission B-scans to assess detectability versus defect type and size. Attenuation correction will not be applied since the Tx-Rx separation is constant.

5.2 MEASUREMENTS ON A FREE PLATE

5.2.1 Line Scan across the Plate Width

To assess the feasibility of guided-wave EMAT inspection for leakage localization, a 3-mm austenitic stainless plate (EN 1.4307/AISI 304L, 390 × 290 × 3 mm) was fabricated with four through-thickness defects arranged along the midline (Figure 33). All defects were produced by electrical discharge machining and represent leakage-type flaws: (A) a Ø1 mm circular hole; (B) an oblique slot 10 mm long with 1 mm opening at 30° to the scan axis; (C) a straight slot 10 mm long with 1 mm opening; and (D) a straight slot 10 mm long with 0.25 ± 0.05 mm opening. Defects are spaced by 80 mm with 60 mm edge margins.

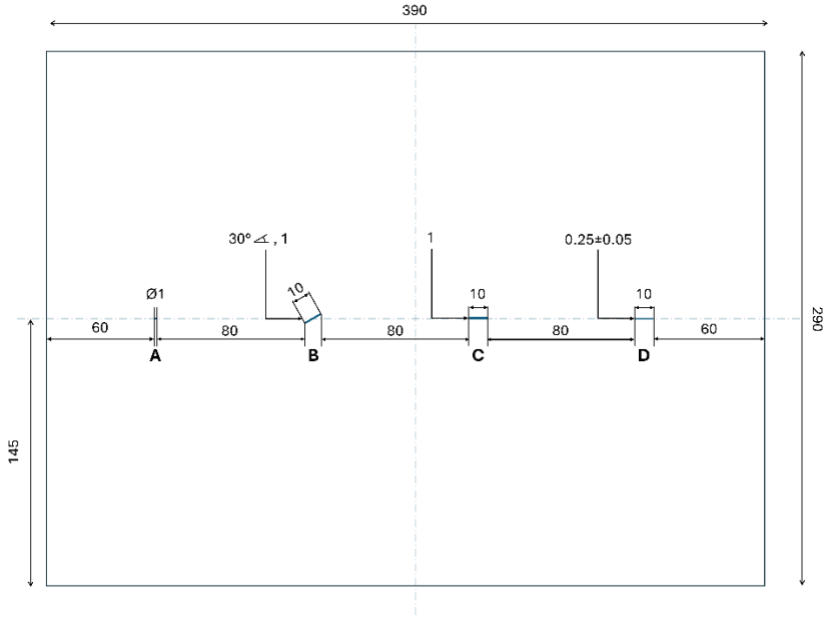

Figure 33. Schematic of the plate specimen. Material: EN 1.4307 (AISI 304L). All defects are through wall. All dimensions are in mm, and the plate was 3 mm thick.

The scan was performed across the plate using a Tx-Rx separation of 80 mm and a scan step of 5 mm between each measurement point along the plate width. The Tx-Rx separation of 80 mm was selected based on the observed low attenuation of the guided waves and to ensure a sufficiently developed wavefield, and temporal separation of the slower SH1-mode at the receiver location.

The chosen scan step represents a compromise between spatial resolution and total scanning time and is of the same order of magnitude as the dominant wavelength of the guided waves used.

Given the measurement geometry and the characteristic wavelength of the guided waves, minor variations in the scan step are not expected to significantly influence the localization results.

The measurements started 5 mm from the leftmost edge in Figure 34 and ended at 355 mm for a total of 71 measurement points along the scanning axis (x). The dimensions are given with respect to the probe's left edge, consequently, the center positions of the sensors range from 20 to 375 mm (the probes are 30 mm wide). The remaining setup was identical to that used for the attenuation and velocity estimation measurements described in Sect. 5.1.3.

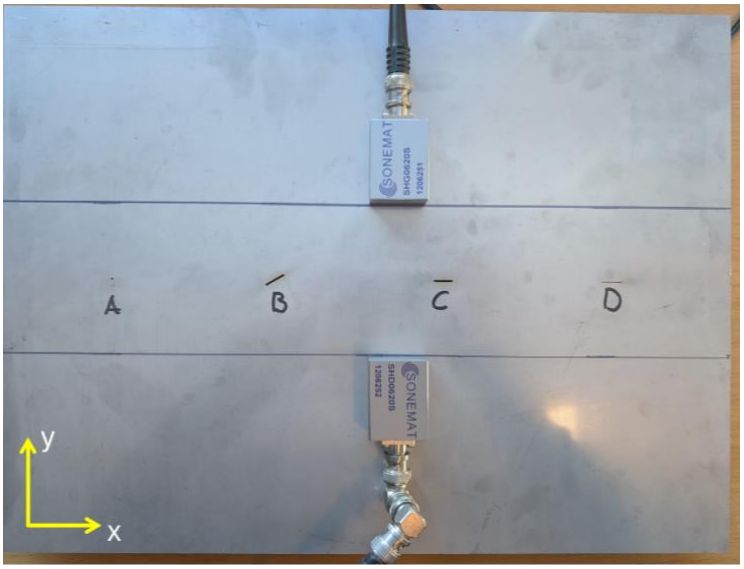

Figure 34. Austenitic steel plate with defects showing sensor placement for the line scan. The upper probe is Tx, lower Rx and the separation between them were 80 mm. Guided SH wave propagation in y-direction and particle displacement in x.

The raw time records were converted to A-scans and then assembled into a transmission B-scan (time × scan position). Each A-scan was processed as follows: (i) zero-phase band-pass filtering around the 600 kHz centre, (ii) removal/blanking of the early EM crosstalk gate, (iii) time referencing using the calibration constants (t_0, c_s) so that the SH0 arrival is aligned across positions, and (iv) formation of the analytic signal via the Hilbert transform and extraction of its envelope. Because the Tx–Rx separation was constant (80 mm), no range-loss (attenuation) correction was applied. A representative A-scan from the first position is shown in Figure 35 together with its envelope. Two distinct peaks are visible: the first corresponds to the non-

dispersive SH0 packet used for imaging, and the second to the slower SH1 packet.

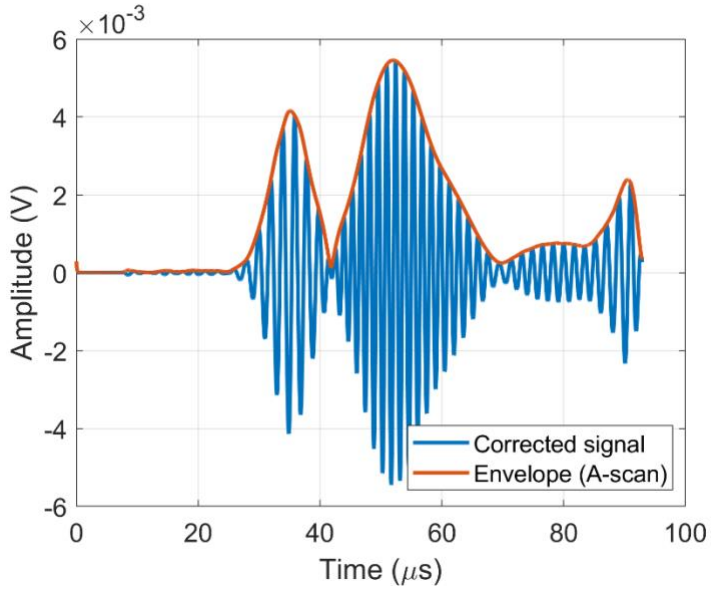

Figure 35. Processed signal (blue) and its envelope (orange) which forms an A-scan.

The B-scan in Figure 36 shows both wave packets and three out of the four defects are clearly indicated by the scan. The SH0 amplitude does appear less stable than the SH1 which is why it is beneficial to include this second mode although unintentionally generated. The variability in amplitude is likely caused by inconsistency in probe positioning, which could be mitigated using tailored probe manipulators. Another way to mitigate the amplitude variation is to smooth the signal using two-dimensional Gaussian filtering of the image. This reduces the sharp variations but also reduces the defect-induced attenuation. The smoothed and SH0-gated B-scan is shown in Figure 37 with the expected defect positions being annotated in red.

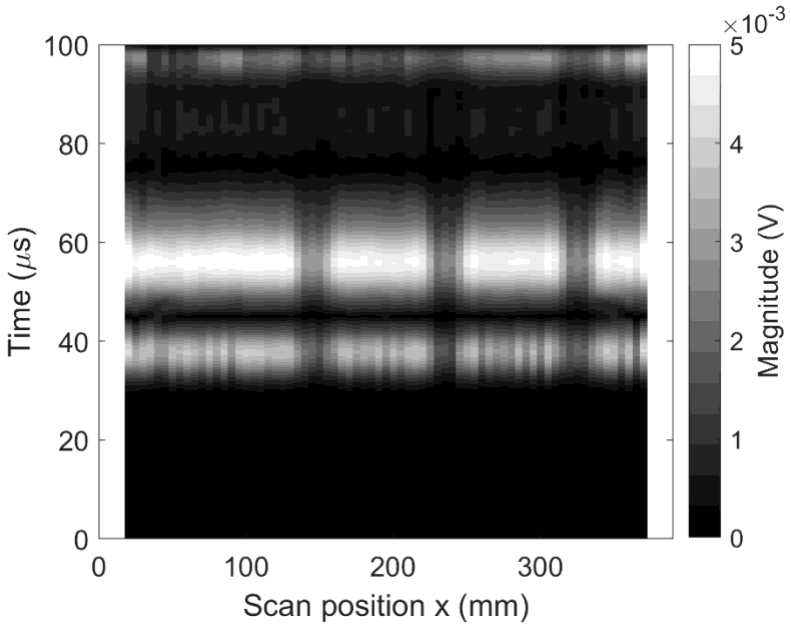

Figure 36. B-Scan from filtered signals.

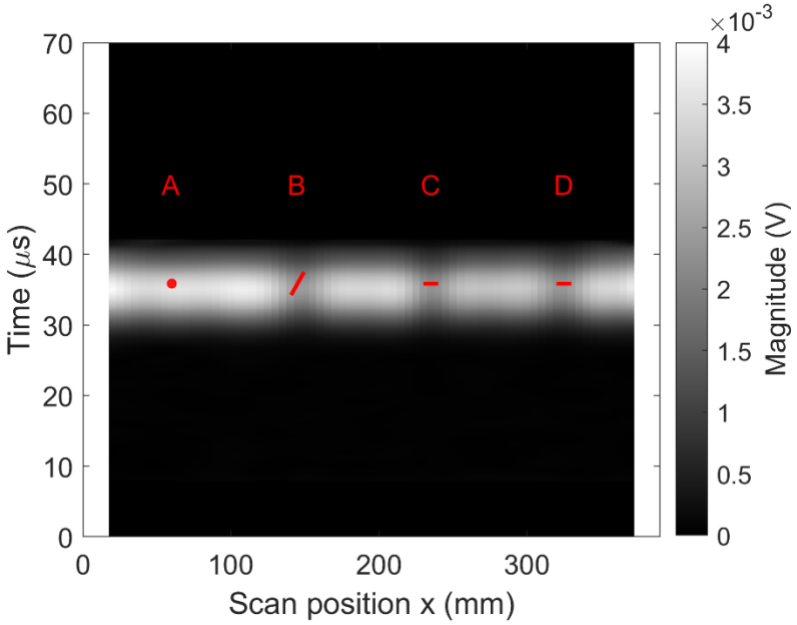

Figure 37. SH0-gated B-scan smoothed using 2-D Gaussian filtering. Defects annotated in red.

While the B-scans give clear indications on three of the four, it can be difficult to evaluate the impact of the defects on the signal strength due to the grey scale. By plotting the maximum magnitude across the SH0 profile, as in Figure 38, the magnitude drop becomes clear and

positioning the defects is more precise. By studying this figure, it is evident that the 1 mm hole cannot be resolved while the other defects are clearly detected and precisely *located*.

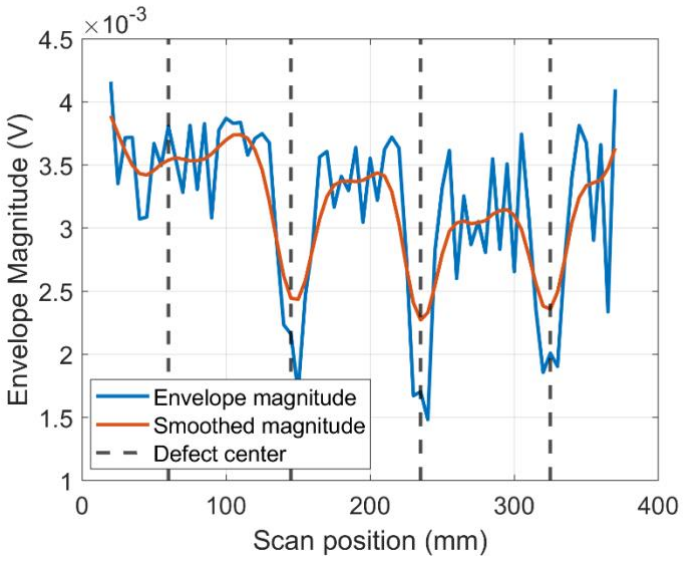

Figure 38. Maximum envelope magnitude for SH0 using filtered (blue) and smoothed (orange) signal. Dashed lines indicate the center position of the defects.

The results demonstrate that shear-horizontal guided waves generated by EMATs can produce clear indications when the inspection geometry is favourable. In the present orientation, the defects present a large effective footprint along the scan axis, which aids visibility. However, the ultrasonic "shadow" is strongly azimuth dependent. When the defect faces align unfavourably with the SH particle motion, contrast can be markedly reduced. To quantify this effect, the next section presents scans taken orthogonal to the current line. This rotation minimizes the footprint for the longitudinal slots, while the oblique slot and the circular hole are expected to be largely unaffected.

5.2.2 Orthogonal Scan (90° rotation)

Defect orientation (azimuth) controls both the contrast and the spatial footprint of the indication in ultrasonic imaging. For SH0, the least favourable case occurs when the slot is aligned with the SH0 particle motion (i.e., crack faces parallel to displacement), which yields weak scattering even if the footprint is large along the scan. Conversely, when displacement is perpendicular to the crack faces, the contrast

increases, although the footprint may be narrow if the scan only crosses the defect opening. An axisymmetric hole is essentially independent of orientation. To evaluate orientation effects and establish a worst-case baseline, the widthwise line scan (see Figure 34) was complemented by orthogonal scans, i.e., rotated 90° relative to the original direction. The scan orientation (y) is illustrated in Figure 39.

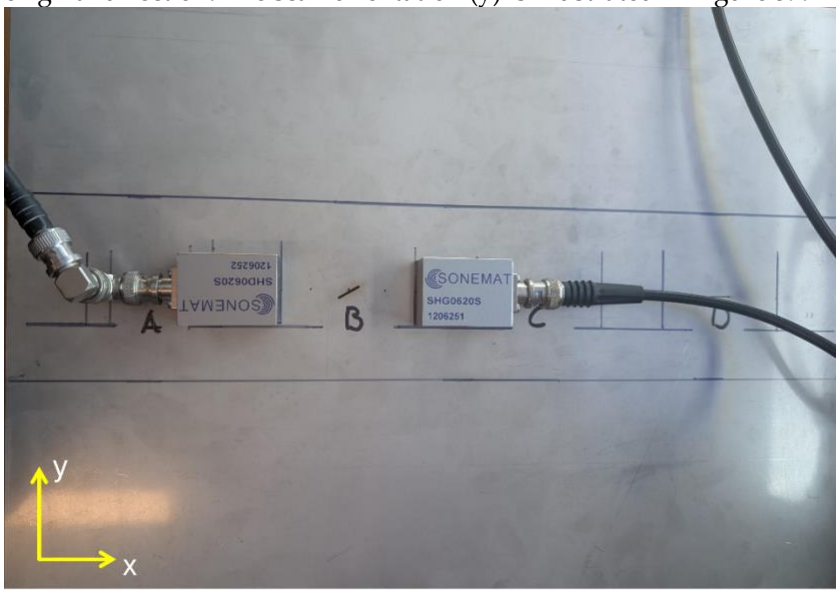

Figure 39. Rotated scan between defects. Guided SH wave propagation in x and particle displacement in y.

For each defect, a one-dimensional scan was acquired with the same instrumentation and 5 mm step but a Tx–Rx separation of 60 mm. Each scan line spanned 110 mm (x = 15–125 mm), yielding 23 positions per defect, with the defect centroid at x = 70 mm. Although the hole and the oblique slot are expected to be largely insensitive to scan direction, their results are included for completeness and for direct comparison with the longitudinal slots, which represent the most unfavourable inspection geometry in this context due to their limited footprint.

Figure 40 shows the B-scan across defect A (Ø1 mm hole). As anticipated, rotating the scan and reducing the Tx–Rx spacing to 60 mm do not improve detectability and the SH0 packet exhibits no distinct shadow. Resolving such a small, axisymmetric feature would require a shorter wavelength (higher centre frequency and/or different EMAT design). Driving the present EMATs far from their design frequency would demand higher power and longer tone

bursts, which increases mode overlap and interference with SH1, complicating interpretation. The receiver would also be insensitive to higher frequencies which makes it unfeasible to simply increase the frequency.

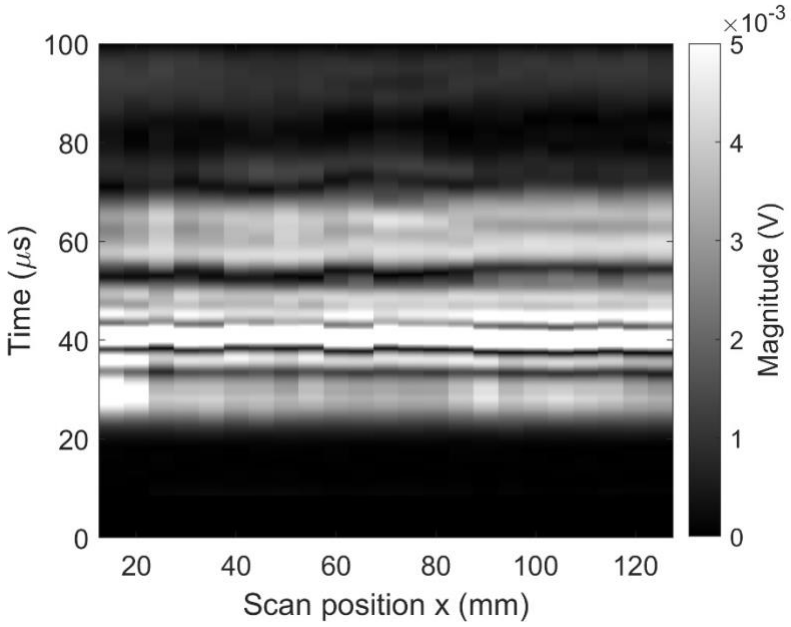

Figure 40. B-scan across defect A. Defect center is at x = 70 mm. No indication.

For the oblique slot B, the corresponding B-scan in Figure 41 shows a clear amplitude reduction at the defect location, consistent with expectations for a slot that is not aligned with the SH0 particle motion and its unaffected footprint.

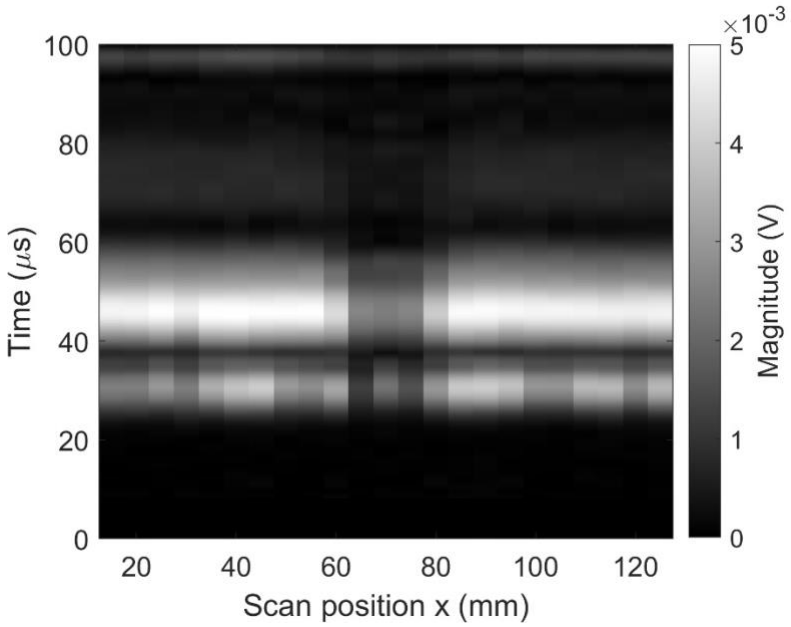

Figure 41. B-scan across defect B. Defect center is at x = 70 mm. Clear indication.

Figure 42 shows the transmission B-scan over defect C (10 mm × 1 mm slot). In the SH0 wave packet, the scan reveals local minima at each side of the defect and a maximum at the expected center position of the defect. This is even more apparent in the line of maximum envelope across the profile (Figure 43). The local maximum likely arises from constructive interference of edge-diffracted SH0 waves. The modest contrast is attributed to the small footprint of the defect (1 mm compared to 10 mm in the former case).

Because the slot is favourably oriented (SH particle motion perpendicular to the slot faces), both modes should interact with the defect. However, the later-arriving SH1 packet shows a much clearer amplitude drop. This stronger SH1 response is consistent with the mode shape expressions in Eq. (1) (see also Figure 6 (c)). Although both modes strain along the propagation direction ($\gamma_{xy} = \partial u_x/\partial z$), they differ in their through-thickness behaviour. SH0 has a constant displacement ($m = 0$ in (1)), giving $\gamma_{zy} = \partial u_y/\partial z = 0$, and therefore only modest interaction with surface-breaking defects. In contrast, SH1 exhibits strong variation at the surfaces, producing large through-thickness shear strain (γ_{zy}) exactly where the surface crack perturbs the field most strongly. This leads to the more pronounced SH1 indication observed in the B-scan.

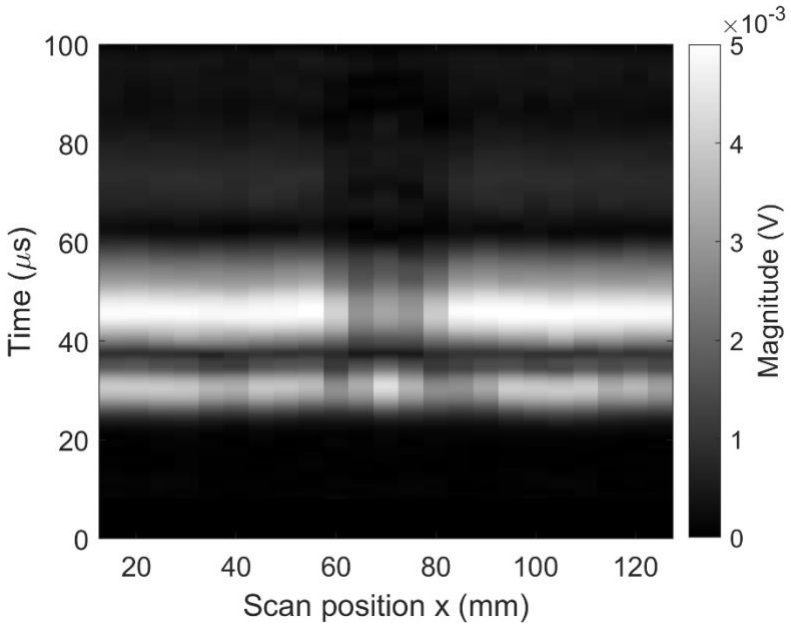

Figure 42. B-scan across defect C. Defect center at x = 70 mm. Indication on SH1 wave-packet.

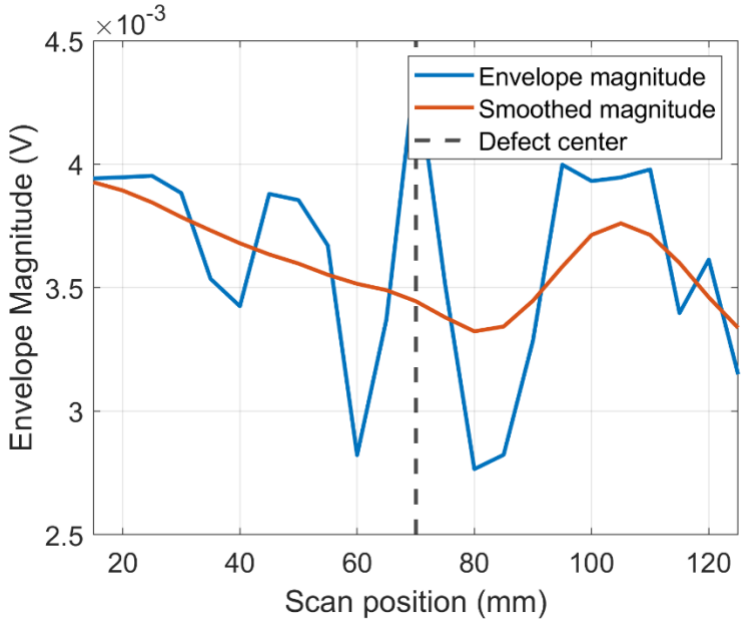

Figure 43. Maximum magnitude for the SH0 wave-packet for defect C.

Figure 44 shows the transmission B-scan over defect D (10 mm slot, 0.25 ± 0.05 mm opening). Analogous to defect C (Figure 42), the B-scan shows local indications with minima on each side and a ridge in the expected center position. The effect is, once again, clearer in the

line of maximum envelope across the profile (Figure 45), which shows a shallow central maximum bounded by symmetric dips. In the later SH1 gate the defect produces a clear ultrasonic shadow, analogous to defect C. This highlights a successful case of exciting higher-order modes at a frequency which maintains good separation of the wave packets. If a higher frequency was excited, then SH1 group velocity would approach c_s and interfere with SH0.

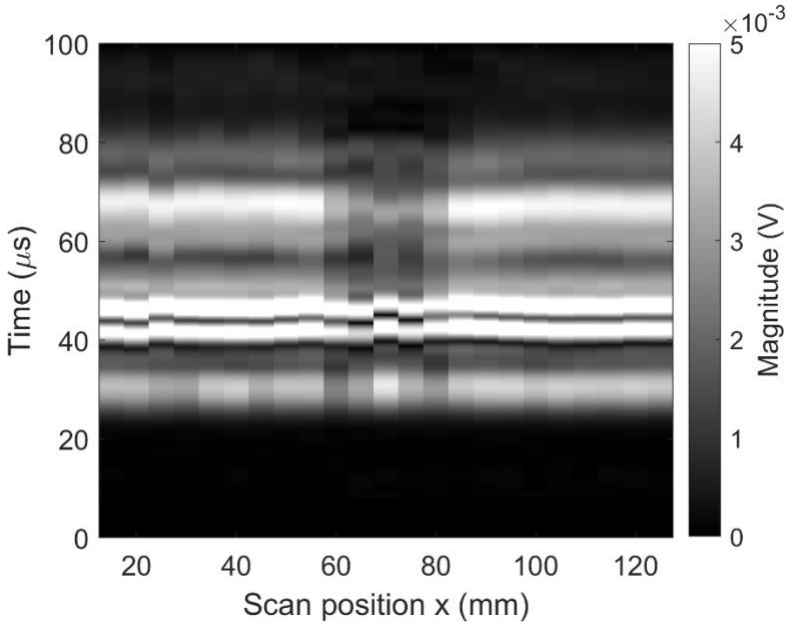

Figure 44. B-scan across defect D. Defect center at x = 70 mm. Indication on SH1 wave-packet.

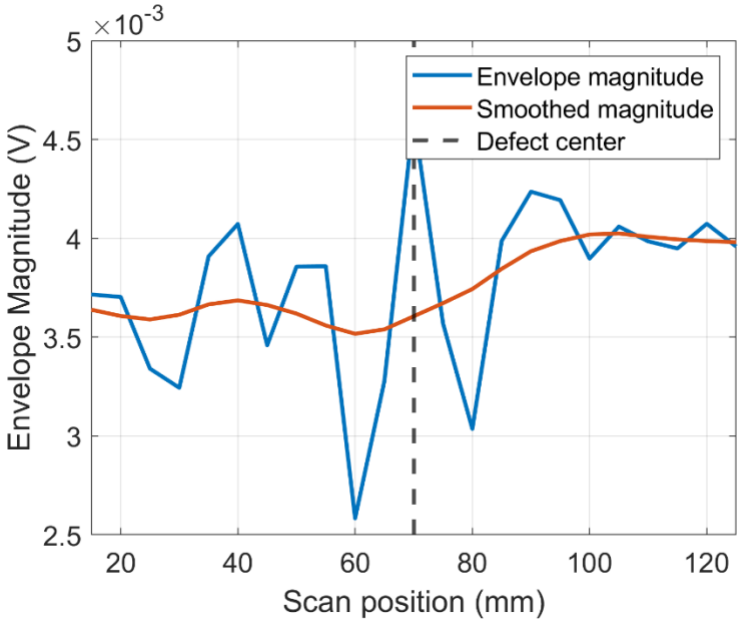

Figure 45. Maximum magnitude of the SH0 wave-packet along the profile for defect D.

5.2.3 Comparison of Widthwise and Orthogonal Scans

The rotated scans on the free plate confirm a clear orientation dependence of the SH0 contrast. Table 1 shows a comparison of the SH0 contrast between the widthwise and orthogonal scans using the smoothed maximum-envelope lines.

For each defect, the reference level A_{ref} is the local baseline taken from the smoothed (to avoid noisy spikes) magnitude in two side windows of each defect (15-30 mm to the left and right of the defect), while the defect level A_{def} is the minimum of the smoothed envelope within a ±5 mm window around the known centre. Contrast is reported as

$$\mathbf{C_{dB}} = \mathbf{20}\boldsymbol{log_{10}}(\frac{\boldsymbol{A_{ref}}}{\boldsymbol{A_{def}}}) \tag{4}$$

And

$$\mathbf{C_{\%}} = \frac{\boldsymbol{A_{ref}} - \boldsymbol{A_{def}}}{\boldsymbol{A_{ref}}} \tag{5}$$

As seen in Table 1, the longitudinal slots (C and D), yields pronounced contrasts of 6.41 dB and 5.63 dB, respectively in the widthwise scan, whereas the orthogonal scan, where the line

intersects only the 1 mm / 0.25 mm openings, reduces the contrast to ≈1–1.4 dB. The oblique slot B (30°) is comparatively azimuth-insensitive (≈6.2–6.4 dB in both orientations), as expected by its unaffected footprint. The 1 mm hole A remains weak overall (0.07 dB widthwise; 1.89 dB rotated). These results show that, for the free plate and current probe configuration, the geometric footprint sampled by the scan strongly affects SH0 indications. Crossing the 10-mm slot length produces robust dips, while crossing only the narrow opening gives marginal contrast. This baseline will be used to interpret the behaviour on the concrete-bonded plate in Sec. 5.3.

Table 1. Defect contrasts from smoothed envelope magnitude of the free plate.

Defect	Orientation	A_{ref} ($\times 10^{-4}$ V)	A_{def} ($\times 10^{-4}$ V)	Contrast (dB)	Contrast (%)
A	Widthwise	35.2	35.1	0.073	0.36
A	Orthogonal	39.3	35.8	1.89	8.99
B	Widthwise	33.1	24.4	6.15	26.5
B	Orthogonal	32.6	23.7	6.39	27.4
C	Widthwise	31.3	22.7	6.41	27.4
C	Orthogonal	35.7	33.8	**1.09**	**5.30**
D	Widthwise	31.3	23.6	5.63	24.5
D	Orthogonal	37.9	35.4	**1.36**	**6.59**

Overall, the results suggest using SH1 as a complementary contrast channel while SH0 provides the non-dispersive timing for imaging, provided the modes are temporally separated. However, it is important to consider that any change in the boundary conditions by, e.g., welding to profiles as viewed in Figure 2, will alter the guided wave dispersion, mode content, and attenuation, so the free-plate calibration does not transfer. To investigate these effects, the next sections will report on experiments on the same plate with concrete backing.

5.3 INSPECTION OF A BONDED PLATE

Guided wave propagation is governed by the geometry and boundary conditions of the host structure. Consequently, their attenuation,

dispersion, and mode content change with geometric changes (e.g., plate thickness) and with constraints at the boundaries. Since the liners are typically anchored to the concrete using steel profiles (e.g., the L-profiles shown in Figure 2), it is essential to understand how such constraints affect signal characteristics compared with a free plate.

To assess the impact of the altered boundary conditions, the same 3 mm EN 1.4307 (304L) plate from Sect. 5.2, was bonded to a concrete block by mixing a cement slurry with w/c-ratio of 0.40. The bond was cured for 7 days before the experiment was initiated. The setup can be viewed in Figure 46, which was identical to the previous experiment except for the pre-amplifier gain, which was increased from 20 dB to 30 dB to compensate for the expected losses from the bond.

Although a concrete bond is not identical to the dissimilar-metal welds expected in nuclear pool liners, it provides a controlled, uniform way to study bond-induced boundary effects, such as changes in dispersion, mode content, and attenuation, without the geometric and metallurgical complexity of real weldments.

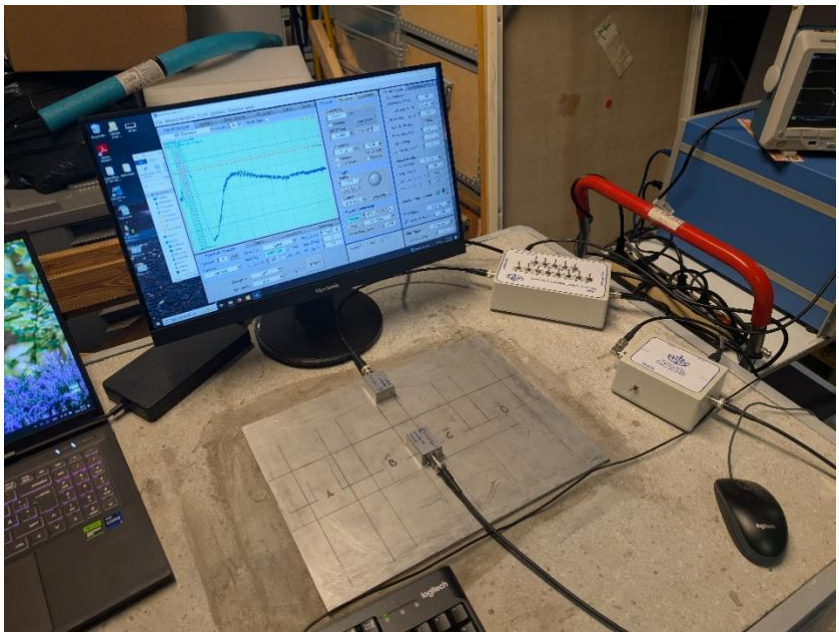

Figure 46. Experimental setup. The plate is attached to the concrete using a cement slurry.

5.3.1 Attenuation Estimation of the Concrete-bonded Plate

The attenuation per unit length was estimated analogously to Sect. 5.1.3. The Tx-Rx separation spanned 50–100 mm (here in 5 mm steps). For each position, the RMS envelope amplitude of the first arrival was referenced in dB and regressed against separation using Eq. (2),

Figure 47 shows the data and linear fit, yielding α = 0.149 dB/mm (R^2 = 0.873). Compared with the free-plate value α = 0.039 dB/mm, the concrete backing increases attenuation by a factor of ≈ 3.8. At the nominal 80 mm inspection range, this corresponds to ≈ 12 dB of path loss (vs ≈ 3.1 dB for the free plate).

This marked increase is consistent with energy leakage into the backing (radiation through the bond layer) together with additional scattering and damping introduced by the constrained boundary. The use of higher pre-amplifier gain was therefore well-motivated.

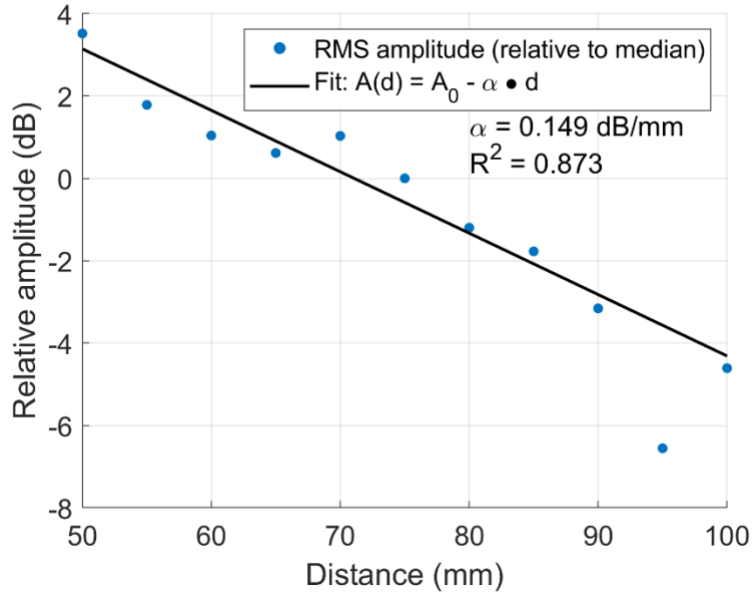

Figure 47. Relative amplitude (in dB) plotted against probe separation. Line fitting gives α = 0.149 dB/mm with a coefficient of determination R^2 = 0.873.

5.3.2 Widthwise Line Scan Across a Concrete-bonded Plate

Transmission B-scans were acquired as described in Sect. 5.2.1 and are shown in Figure 48. The first attempt at bonding the stainless liner plate to the concrete substrate resulted only in a partial bond.

Although unintended, this outcome provided a clear illustration of the effect of liner-concrete contact on guided wave propagation.

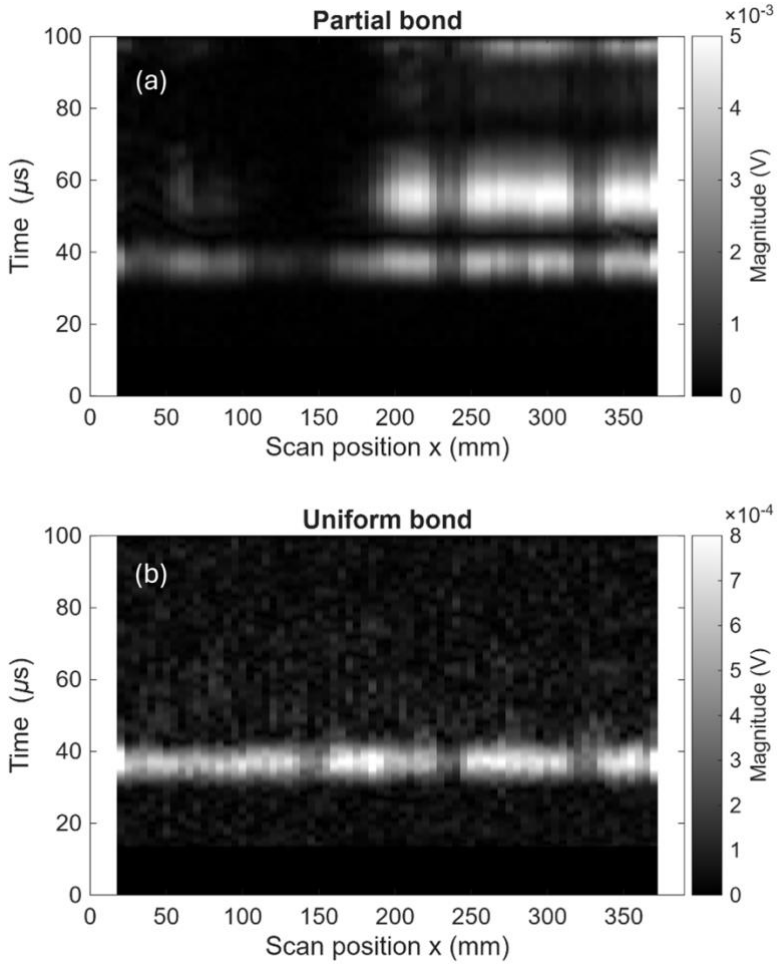

Figure 48. Comparison of transmission measurements obtained for a liner plate bonded to concrete under (a) partially bonded and (b) uniformly bonded conditions. In (a) only part of the plate is mechanically bonded to the concrete substrate, whereas (b) represents uniform bonding over the entire plate area. For the uniformly bonded case, a single SH0 wave packet is observed, while later wave packets present for the free plate are absent due to the changed boundary conditions.

The transmission B-scan in Figure 48 (a) shows a distinct transition along the scanning direction. Within the bonded region, the higher-order packet disappears and only a single SH0 packet remains, while the overall amplitude is reduced due to increased leakage and attenuation. This contrast clearly illustrates how bonding alters the boundary conditions for guided waves and demonstrates that SH-

based scanning can also be used to assess bond condition in addition to detecting discrete flaws.

The effect of bonding is further highlighted in the results obtained for uniform liner-concrete bonding shown in Figure 48 (b). Bonding the plate to concrete breaks the free-surface symmetry and introduces strong radiation (leakage) and damping for higher-order SH modes. As a result, SH0 dominates the received signal while SH1 is either above its effective cutoff for the bonded configuration or is heavily attenuated by leakage into the concrete substrate. Subsequent analysis is performed solely on the data from the uniformly bonded case.

Despite the increased attenuation (Sec. 5.3.1) and the suppression of higher modes, the slots B–D remain detectable in the SH0 gate. This is illustrated in the smoothed B-scan in Figure 49, and is quantified by the maximum-envelope profile in Figure 50, which exhibits pronounced dips at the expected centres. As before, the 1 mm hole (A) shows weak contrast, consistent with previous results.

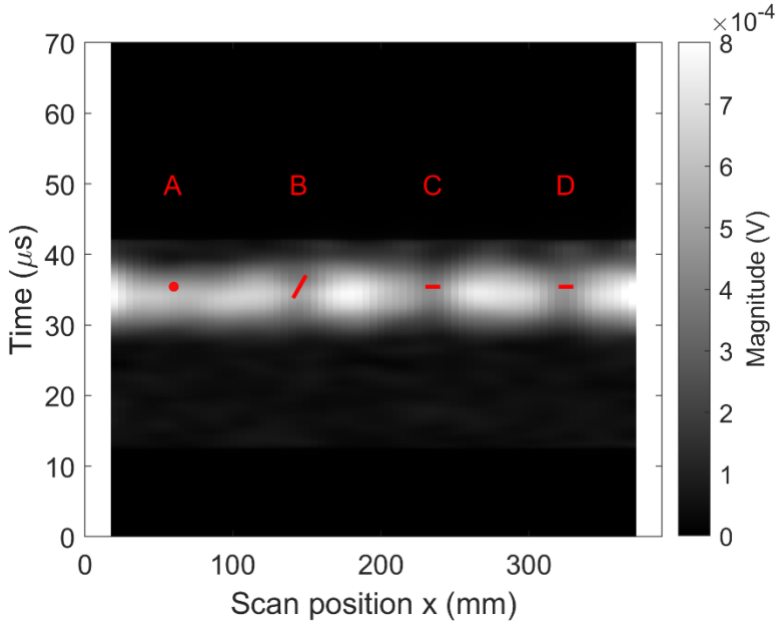

Figure 49. Smoothed B-scan focused on the first arrival. Defects annotated in red.

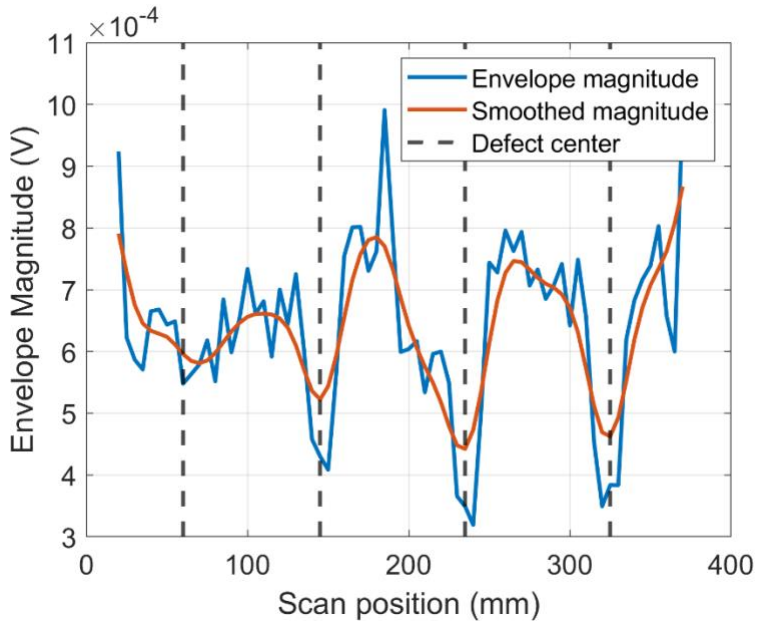

Figure 50. Maximum magnitude along the B-scan profile showing minima at B–D.

Relative to the free-plate baseline, the concrete bond removes the complementary SH1 gate but leaves SH0 essentially unchanged (except for increased attenuation) and maintains usable SH0 contrast for the slots (details quantified in Sec. 5.3.3). Practically, this implies that bonded regions can be inspected with SH0-only processing, provided sufficient front-end gain.

The results clearly indicate the expected outcome that the SH dispersion differs from that of a free plate. This explains the absence of a distinct SH1 packet here. Hence, higher centre frequencies may be used, provided the bonded-plate dispersion (or an empirical check) confirms that higher modes remain leaky/absent. Note that increasing frequency decreases the wavelength but increases attenuation, however, this should not be an issue since it is possible to increase both output power and front-end gain.

5.3.3 Orthogonal Line Scan Results and Contrast Comparison

To assess azimuth effects with the concrete backing, a second set of scans was acquired with the probes rotated by 90° relative to the widthwise line in Sec. 5.3.2. Processing and gating were identical; only the SH0 packet is present, as in the widthwise scan. Contrast was

quantified (Table 2) from the smoothed maximum-envelope line using the same local baseline method as described in 5.2.3.

For the oblique slot B, the orthogonal B-scan (Figure 51) shows a pronounced minimum at the expected position $x = 70$ mm, which is also clear in the envelope profile (Figure 52). The rotated orientation yields higher SH0 contrast than the widthwise scan (7.70 dB vs 5.38 dB in Table 2), likely due to the closer Tx-Rx separation (60 mm vs 80 mm).

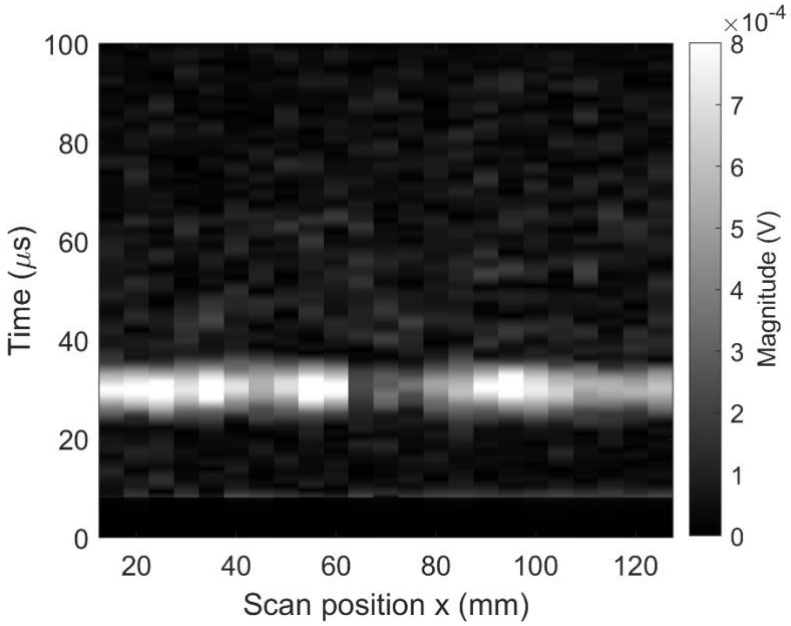

Figure 51. Transmission B-scan for rotated measurements. Defect B is clearly indicated at x = 70 mm.

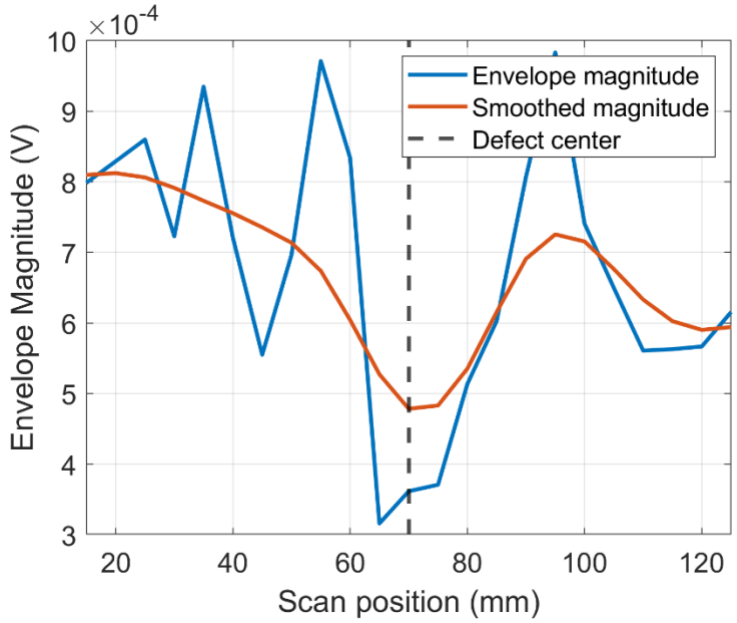

Figure 52. Maximum envelope magnitude for the scan across defect B. Clear indication.

By contrast, the longitudinal slot C exhibits only a weak indication when rotated. The B-scan shows barely any contrast (Figure 53), and the envelope profile confirms a shallow dip (Figure 54). The measured contrast drops from 7.00 dB (widthwise) to 3.27 dB (orthogonal) as highlighted in Table 2. This reduction follows from the small footprint in the orthogonal pass (the scan intersects only the 1 mm opening, not the 10 mm length). A similar trend is observed for slot D (0.25 mm opening), where the contrast decreases from 7.18 dB to 3.75 dB on rotation. The 1 mm hole A remains weak overall and even shows a slight amplitude increase in the rotated case (−1.58 dB).

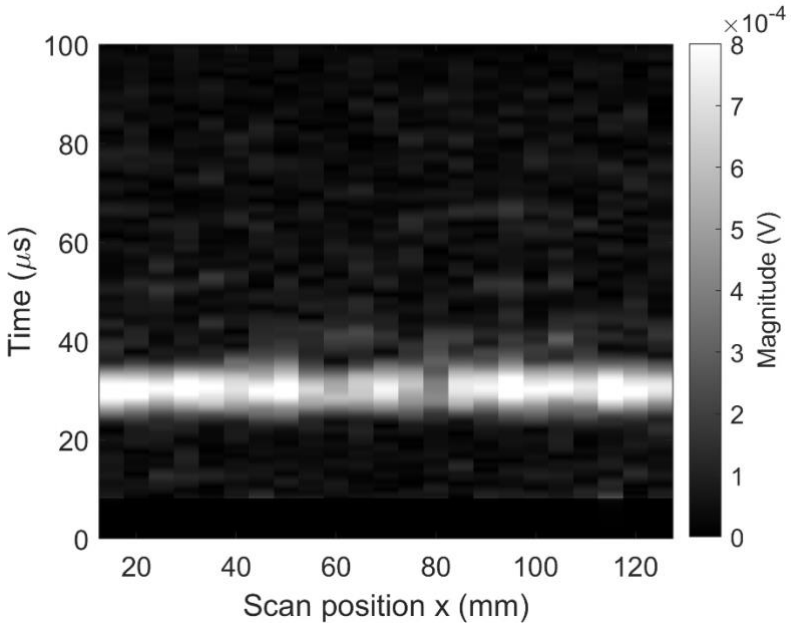

Figure 53. Transmission B-scan for rotated measurements over defect C, no visual indication.

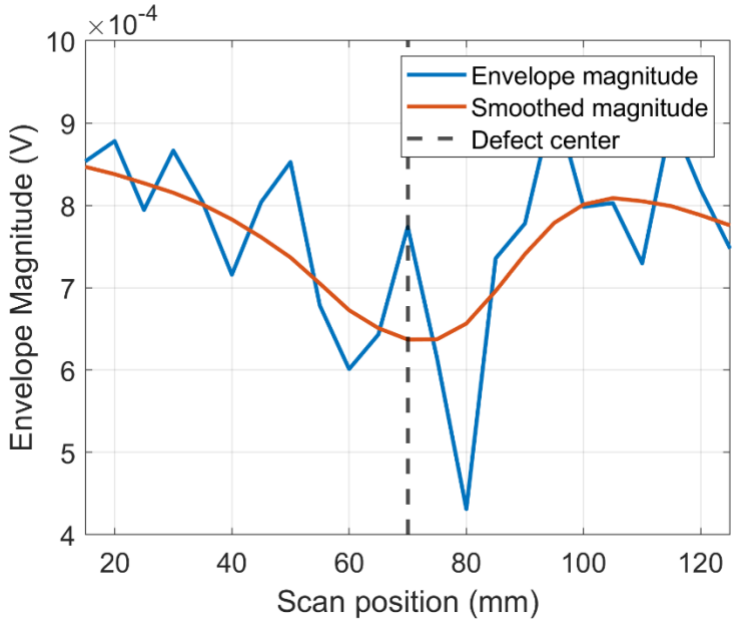

Figure 54. Maximum envelope magnitude for the scan across defect C, weak indication.

Table 2. Defect contrasts from smoothed envelope magnitude of the concrete-bonded plate.

Defect	Orientation	A_{ref} ($x10^{-4}$ V)	A_{def} ($x10^{-4}$ V)	Contrast (dB)	Contrast (%)
A	Widthwise	6.27	5.85	1.38	6.68
A	Orthogonal	7.03	7.60	-1.58	-8.19
B	Widthwise	6.84	5.22	5.38	23.6
B	Orthogonal	7.03	4.78	7.70	32.0
C	Widthwise	6.27	4.42	7.00	29.5
C	Orthogonal	7.50	6.37	**3.27**	**15.1**
D	Widthwise	6.62	4.63	7.18	30.2
D	Orthogonal	6.95	5.76	**3.75**	**17.1**

With concrete backing, where higher-order modes are suppressed, the orientation dependence persists for SH0, and it manifests primarily through the geometric footprint of the scan. Crossing a slot perpendicular to its faces (widthwise) provides stronger contrast than crossing only the narrow opening (rotated). In bonded regions, SH0-only imaging remains effective for narrow slots provided scan paths are planned to intersect suspected slot azimuths transversely. When azimuth is unknown, orthogonal passes or small-angle sweeps are recommended.

5.4 CONCLUSIONS FROM THE EMAT EXPERIMENTS

The experiments show that EMAT-launched SH waves enable contactless imaging on stainless plates. The fundamental SH0 mode provides clean and robust transmission B-scans; narrow slots (10×1 mm and 10×0.25 mm) are consistently detected, and on free plates a later SH1 mode can add useful contrast when geometry is unfavourable for SH0. SH waves are theoretically insensitive to water and EMATs require no couplant, which simplifies deployment and reduces variability.

It should be noted that the artificial defect sizes used in the EMAT experiments were selected to demonstrate mechanisms and scan behaviour at a controlled SNR and geometry, rather than to represent the smallest leak-equivalent apertures. The experiments therefore do not aim to establish absolute detection limits for the smallest possible

leaks, which would require dedicated studies beyond the scope of the present work.

When the plate is bonded to concrete, higher-order modes are suppressed, yet SH0 remains effective. Transmission B-scans still show clear minima over slots, albeit with higher attenuation that is manageable with modest extra gain. Contrast is governed mainly by polarization and scan footprint: it is strongest when SH particle motion is perpendicular to the slot faces and the line scan crosses the slot length, and much weaker when the scan crosses only the narrow opening.

Operationally, EMATs are quick to use and pair well with short bursts, but they are frequency-selective, so higher resolution demands different probes and typically more drive power, while attenuation rises with frequency. The dispersion analysis (Figure 55) captures the trade-off well: increasing frequency shortens wavelength (better resolution) but on free plates moves higher modes (SH1–SH3 illustrated) well above cutoff and risks multi-mode interference. Bonding the plate alters the boundary conditions, so higher modes are leaky/suppressed, enabling SH0-only imaging at higher frequencies, at the cost of greater loss and tighter probe design.

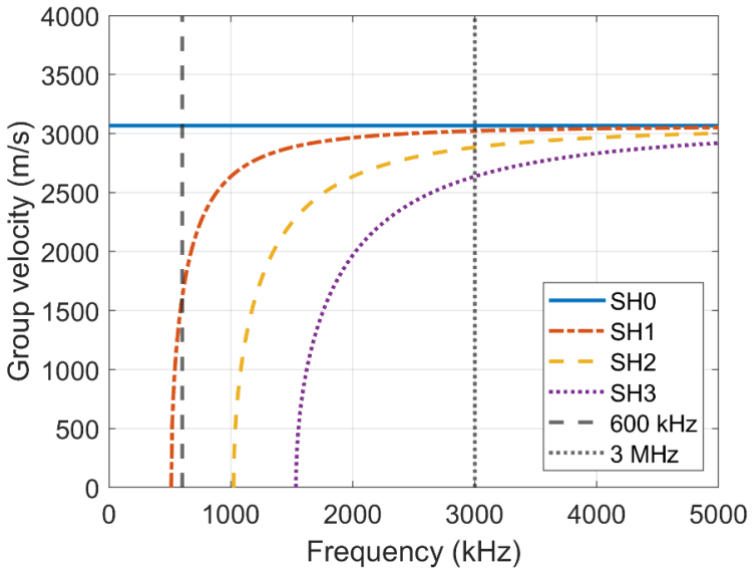

Figure 55. Analytic group velocity (Eq. (3)) for a 3 mm stainless steel plate with up to third-order modes. Frequencies corresponding to 600 kHz (~5mm wavelength) and 3 MHz (~1 mm wavelength) are highlighted with vertical dashed lines.

In practice, SH-EMAT proved to be a robust option for couplant-free screening and for detecting slots. However, achieving sub-millimetre spatial resolution is challenging due to increased attenuation and the onset of multi-mode interference at higher frequencies, particularly on free plates. While greater probe separation can help preserve temporal separation of wave packets, these limitations constrain the applicability of SH-EMAT for high-resolution localization of leakage-relevant defects. SH-EMAT is therefore best positioned as a complementary, screening modality for selected scenarios. It is not prioritized as the primary route for leakage localization compared with ACFM (primary) and PAUT (secondary).

6 Conclusions

This work set out to evaluate practical, remotely deployable methods for locating small, leakage-relevant defects in thin austenitic stainless-steel liners. The study combined controlled trials on a machined 3-mm EN 1.4307 (304L) plate (free and concrete-bonded) with an emphasis on shear-horizontal (SH) guided waves generated by EMATs. Emphasis was placed on understanding the capabilities and limitations of SH guided waves generated by EMATs.

The results demonstrate that EMAT-launched SH waves enable contactless inspection of stainless steel without couplant and that the non-dispersive SH0 mode at 600 kHz provided clean timing and robust transmission B-scans. Narrow slots (10×1 mm and 10×0.25 mm) were consistently detected. On free plates, a later SH1 packet was often observed and provided useful complementary contrast. When the plate was bonded to concrete, higher-order SH modes were suppressed, yet SH0 remained usable and slot indications persisted, albeit with higher attenuation that is manageable with additional front-end gain.

Two factors dominated contrast: (i) the alignment of SH particle motion relative to defect faces (polarization/orientation), and (ii) the scan footprint. Indications were strongest when particle motion was perpendicular to slot faces and the scan crossed the slot length; crossing only the opening yielded weaker dips even in favourable polarization. Axisymmetric holes below the present wavelength (~5 mm) produced essentially no responses. These behaviours were consistent across free and bonded configurations once differences in attenuation and mode content were accounted for.

The dispersion analysis clarifies the central trade-off for SH-based inspection: higher frequency improves spatial resolution but increases attenuation and, for free plates, brings multiple SH modes above cutoff, raising the risk of multi-mode interference. Bonding alters the boundary conditions, so higher modes become leaky/suppressed, enabling SH0-only imaging at elevated frequencies. From a physical standpoint, this makes SH-EMAT attractive for couplant-free screening and for detecting narrow, elongated defects, particularly in bonded regions, given that higher frequencies can be used. However, achieving sub-millimetre defect sizing on free plates remains challenging and would require complementary techniques.

SH guided waves are theoretically insensitive to fluid loading due to their in-plane particle motion. While this assumption is well established, no dedicated underwater verification was performed within the present study, as SH-based methods were not pursued as the primary direction for further development.

From an application and inspection-planning perspective, a balanced inspection portfolio is therefore recommended. Alternating Current Field Measurement (ACFM) emerges as the most promising near-term technique for localizing surface-breaking cracks relevant to leakage, owing to its tolerance to lift-off and coatings, demonstrated underwater performance, and direct sizing capability based on Bx/Bz response without calibration blocks. Phased Array Ultrasonic Testing (PAUT) should be pursued in parallel where quantitative imaging, weld interrogation, and defect characterization are required; modern array systems and reconstruction methods (TFM, PWI, SAFT) are compatible with submerged robotic deployment and thin plate geometries.

In this context, SH-EMAT is best regarded as a complementary screening technique rather than a primary localization tool and is therefore de-prioritized relative to ACFM and PAUT. Conventional Acoustic Emission and Eddy Current Testing are likewise de-prioritized for leakage localization in this application. Visual testing and photogrammetry should be employed as screening and documentation tools to guide and contextualize subsequent NDT inspections.

7 Recommendations

Alternating Current Field Measurement (ACFM) is the most promising near-term technique for localizing leakage-relevant, surface-breaking flaws on thin austenitic liners. It is inherently tolerant to lift-off and coatings, requires minimal surface preparation, and has been demonstrated in underwater and nuclear contexts, including robotic or crawler-based deployment in constrained geometries. Its Bx/Bz response enables direct sizing without calibration blocks, making it well suited for large area scanning with consistent results.

For ACFM applied to liner plates in pool environments, further work is recommended to systematically evaluate practical detection limits under conditions representative of nuclear facilities. This should include controlled experiments with surface-breaking defects of varying length and depth in thin austenitic liners, covering both laboratory and submerged conditions. Key parameters to investigate include probe design and excitation frequency, probe lift-off and standoff stability under water, surface condition (e.g. coatings and oxide layers), and scanning speed.

Once practical limitations and suitable operating parameters have been established, a focused ACFM pilot with robotic delivery (wall crawler or ROV tool skid) is recommended. The pilot should cover weld toes, heat-affected zones, corners, and attachments, with acceptance criteria tied to minimum reliably detected crack length and depth. It should also include a feasibility check for potential field effects from magnetite aggregates in concrete and a lift-off robustness test at representative standoff.

Further work should address practical implementation aspects for large-area liner inspections, including definition of scan patterns, coverage strategies, and edge handling near weld toes, corners, and attachments. Repeatability studies using multiple operators and repeated scans under submerged conditions are recommended to quantify measurement variability and to support the development of inspection procedures suitable for field deployment.

Phased Array Ultrasonic Testing (PAUT) should be pursued in parallel where quantitative imaging, flaw characterization, and weld interrogation are required. A targeted feasibility study should select

transducers optimized for submerged use, validate coupling and scanning on thin stainless steel plates, and benchmark imaging performance on representative weld mock-ups, including corner and attachment details.

Given the large data volumes expected from robotic ACFM and PAUT inspections, further work is recommended to develop structured data interpretation and decision-support workflows. This includes standardized reporting of indications, confidence grading, and integration with plant documentation to support traceability, re-inspection planning, and long-term condition tracking.

For robotic deployment, further studies should assess mechanical stability, positioning accuracy, and probe force control during vertical and overhead scanning. The influence of speed, surface curvature, and attachment geometry on data quality should be evaluated to define practical operating ranges.

The development and use of representative liner mock-ups, including realistic welds, attachments, and artificial defects, is recommended to support benchmarking, training, and procedure qualification.

8 References

[1] H. J. L. S. R. H.-P. Seifert, "Thermo-Mechanical and Isothermal Low-Cycle Fatigue Behavior of Type 316L Stainless Steel in High-Temperature Water and Air," *Corrosion,* vol. 69, no. 10, pp. 1012 – 1023, 1 October 2013, doi: https://doi.org/10.5006/0875.

[2] *Non-destructive testing – Leak testing – Criteria for method and technique selection (EN 1779)*, EN 1779, CEN, 1999.

[3] A. A. Deev, P. A. Kuznetcov, and S. N. Petrov, "Anisotropy of Mechanical Properties and its Correlation with the Structure of the Stainless Steel 316L Produced by the SLM Method," *Physics Procedia,* vol. 83, pp. 789–796, 2016, doi: 10.1016/j.phpro.2016.08.081.

[4] C. Boller, S. Pudovikov, and A. Bulavinov, "Quantitative ultrasonic testing of acoustically anisotropic materials with verification on austenitic and dissimilar weld joints," 2012.

[5] C. G. Fountzoulas, "Simulated Construction of FeMnAlC Alloy System Phase Diagram and Study of Its Dynamic Characterization," in *Dynamic Behavior of Materials, Volume 1*, (Conference Proceedings of the Society for Experimental Mechanics Series, 2021, ch. Chapter 10, pp. 55–57.

[6] B. Wan, B. Hu, Y. Li, and Y. Zhu, "Study on Effect of Electromagnetic Characteristics of Deformed 304 Stainless Steel on Eddy Current Testing," in *Electromagnetic Non-Destructive Evaluation (XXIII)*, (Studies in Applied Electromagnetics and Mechanics, 2020.

[7] A. J. Sedriks and O. S. Zaroog, "Corrosion of Stainless Steels☆," in *Reference Module in Materials Science and Materials Engineering*, 2017.

[8] S. Jin, X. Sun, and Z. Luo, "Reducing Dead Zone in Ultrasonic Time-of-Flight Diffraction (TOFD): A Review," *Russian Journal of Nondestructive Testing,* vol. 60, no. 2, pp. 170–187, 2024, doi: 10.1134/s1061830923601265.

[9] F. Wang, S. Zhang, M. Sun, and T. Kundu, "Nonlinear ultrasonic C-scan imaging based on sideband peak intensity for fatigue damage evaluation," *NDT & E International,* 2025, doi: 10.1016/j.ndteint.2025.103577.

[10] D. J. Naus, B. R. Ellingwood, and H. L. Graves, "Methods for assessing NPP containment pressure boundary integrity," *Nuclear Engineering and Design,* vol. 228, no. 1-3, pp. 55–72, 2004, doi: 10.1016/j.nucengdes.2003.06.024.

[11] A. Abuassal *et al.*, "A Review of Recent Advances in Unidirectional Ultrasonic Guided Wave Techniques for Nondestructive Testing and Evaluation," *Sensors (Basel),* vol. 25, no. 4, Feb 10 2025, doi: 10.3390/s25041050.

[12] S. Yu *et al.*, "Advancing spacecraft safety and longevity: A review of guided waves-based structural health monitoring," *Reliability*

Engineering & System Safety, vol. 254, 2025, doi: 10.1016/j.ress.2024.110586.

[13] D. J. Naus, "INSPECTION OF NUCLEAR POWER PLANT STRUCTURES – OVERVIEW OF METHODS AND RELATED APPLICATIONS," Materials Science and Technology Division, Oak Ridge National Laboratory, Oak Ridge ORNL/TM-2007/191, May 2009.

[14] T. Hayashi and R. Fujishima, "Defect Detection Using Quasi-Scholte Wave for Plate Loaded with Water on Single Surface," *Materials Transactions*, vol. 57, no. 9, pp. 1602–1608, 2016, doi: 10.2320/matertrans.M2016204.

[15] M. Nilsson, "Nonlinear Ultrasonic Evaluation for Corrosion Assessment of Steel Plates Embedded in Concrete," Doctor of Philosophy Doctoral thesis, Engineering Geology, Lund University, Lund, 2024.

[16] H. Gao, S. M. Ali, B. Lopez, D. O. Thompson, and D. E. Chimenti, "Inspection of Austenitic Weld with Emats," presented at the 36th Annual Review of Progress in Quantitative Nondestructive Evaluation, QNDE, Kingston, RI, United States, 2010.

[17] P.A. Petcher and S. Dixon, "Weld defect detection using PPM EMAT generated shear horizontal ultrasound," *NDT & E International*, vol. 74, pp. 58–65, September 2015, doi: https://doi.org/10.1016/j.ndteint.2015.05.005.

[18] J. L. Rose, *Ultrasonic Guided Waves in Solid Media*. Cambridge University Press, 2014.

[19] B. Z. Pete D. Theobald, Janine Avison, "Couplants and their influece on AE sensor sensitivity," *Journal of Acoustic Emission*, vol. 26, 2008. [Online]. Available: https://www.ndt.net/?id=10884.

[20] P. Zuo, "Underwater quantitative thickness mapping through marine growth for corrosion measurement using shear wave EMAT with high lift-off performance," *Ultrasonics*, vol. 143, p. 107426, Sep 2024, doi: 10.1016/j.ultras.2024.107426.

[21] R. B. Thompson, "Physical Principles of Measurements with EMAT Transducers," in *Ultrasonic Measurement Methods*, vol. 19, (Physical Acoustics: Acoustic Press, 1990, ch. 4, pp. 157 – 200.

[22] S. Choi, H. Cho, and C. J. Lissenden, "Nondestructive inspection of spent nuclear fuel storage canisters using shear horizontal guided waves," *Nuclear Engineering and Technology*, vol. 50, no. 6, pp. 890–898, 2018, doi: 10.1016/j.net.2018.04.011.

[23] S. Choi, H. Cho, M. S. Lindsey, and C. J. Lissenden, "Electromagnetic Acoustic Transducers for Robotic Nondestructive Inspection in Harsh Environments," *Sensors (Basel)*, vol. 18, no. 1, Jan 11 2018, doi: 10.3390/s18010193.

[24] T. Saitoh and A. Ishiguro, "Surface crack detection in a thin plate using time reversal analysis of SH guided waves," *Structural*

Engineering and Mechanics, Vol. 80, No. 3 (2021) 243-251, vol. 80, no. 3, pp. 243–251, 2021, doi: 10.12989/sem.2021.80.3.243.

[25] N. E. Sweeney *et al.*, "In-process phased array ultrasonic weld pool monitoring," *NDT & E International,* vol. 137, 2023, doi: 10.1016/j.ndteint.2023.102850.

[26] B.-t. Jiang, S.-g. Yan, J. Huang, and B.-x. Zhang, "Ultrasonic Total Focusing Imaging of Defects in Anisotropic Austenitic Stainless Steel Weld," presented at the 2020 15th Symposium on Piezoelectrcity, Acoustic Waves and Device Applications (SPAWDA), 2021.

[27] M. J. Ranjbar Naserabadi and S. Sodagar, "Application of Phased Array Ultrasonic Transducers for Guided Wave Scanning of Plates Using Multi-point Focusing Technique," *Journal of Nondestructive Evaluation,* vol. 41, no. 2, 2022, doi: 10.1007/s10921-022-00867-0.

[28] G. D. Connolly, Lowe, M.J.S., Rokhlin, S.I., Temple, J.A.G., "Imaging of defects within austenitic steel welds using an ultrasonic array," presented at the Ultrasonic Wave Propagation in Non Homogeneous Media, 2009.

[29] S. Dugan and S. Wagner, "Ultrasonic inspection of austenitic stainless steel welds with artificially produced stress corrosion cracks," 2014.

[30] S. Kumar, M. Menaka, and B. Venkatraman, "Simulation and experimental analysis of austenitic stainless steel weld joints using ultrasonic phased array," *Measurement Science and Technology,* vol. 31, no. 2, 2020, doi: 10.1088/1361-6501/ab48a3.

[31] T. Han, F. Schubert, S. Hillmann, and N. Meyendorf, "Phased array ultrasonic testing of dissimilar metal welds using geometric based referencing delay law technique," presented at the Smart Materials and Nondestructive Evaluation for Energy Systems 2015, 2015.

[32] I. Virkkunen, T. Koskinen, and O. Siljama, "Virtual round robin 2 – Phased array inspection of dissimilar metal welds," *Nuclear Engineering and Design,* vol. 414, 2023, doi: 10.1016/j.nucengdes.2023.112555.

[33] G. Sorger, I. Virkkunen, and C. Söderholm, "Flaw sizing with plane wave imaging (PWI) – total focusing method (TFM) and deep learning for reactor pressure vessel," *NDT & E International,* vol. 153, 2025, doi: 10.1016/j.ndteint.2025.103332.

[34] M.-j. Jung, B.-c. Park, J.-h. Bae, and S.-c. Shin, "PAUT-based defect detection method for submarine pressure hulls," *International Journal of Naval Architecture and Ocean Engineering,* vol. 10, no. 2, pp. 153–169, 2018, doi: 10.1016/j.ijnaoe.2017.06.002.

[35] F. Hu, H.-y. Gou, H.-z. Yang, H. Yan, Y.-q. Ni, and Y.-w. Wang, "Automatic PAUT crack detection and depth identification framework based on inspection robot and deep learning method," *Journal of Infrastructure Intelligence and Resilience,* vol. 4, no. 1, 2025, doi: 10.1016/j.iintel.2024.100113.

[36] E. Patricio Rodrigues, T. Francisco de Oliveira, M. Yassunori Matuda, and F. Buiochi, "Development of a 2-D Array Ultrasonic Transducer for 3-D Imaging of Objects Immersed in Water," *Sensors (Basel),* vol. 21, no. 10, May 18 2021, doi: 10.3390/s21103501.

[37] *Non-destructive testing of welds - Ultrasonic testing - Use of automated phased array technology for thin-walled steel components (ISO 20601:2018)*, E. C. f. S. (CEN), Brussels, Belgium, 2018.

[38] L. Calabrese, L. Bonaccorsi, E. Proverbio, D. Di Pietro, and F. Cappuccini, "SCC damage evolution on martensitic stainless steel by using acoustic emission technique," *Corrosion Engineering, Science and Technology,* vol. 50, no. 5, pp. 364–371, 2014, doi: 10.1179/1743278214y.0000000230.

[39] F. Delaunois, A. Tshimombo, V. Stanciu, and V. Vitry, "Monitoring of chloride stress corrosion cracking of austenitic stainless steel: identification of the phases of the corrosion process and use of a modified accelerated test," *Corrosion Science,* vol. 110, pp. 273–283, 2016, doi: 10.1016/j.corsci.2016.04.038.

[40] Y. P. Kim, M. Fregonese, H. Mazille, D. Féron, and G. Santarini, "Ability of acoustic emission technique for detection and monitoring of crevice corrosion on 304L austenitic stainless steel," *NDT & E International,* vol. 36, no. 8, pp. 553–562, 2003, doi: 10.1016/s0963-8695(03)00065-3.

[41] C. K. Lee *et al.*, "Acoustic emission from pitting corrosion in stressed stainless steel plate," *Corrosion Engineering, Science and Technology,* vol. 43, no. 1, pp. 54–63, 2008, doi: 10.1179/174327808x286176.

[42] X. Cui, Y. Yan, M. Guo, X. Han, and Y. Hu, "Localization of CO(2) Leakage from a Circular Hole on a Flat-Surface Structure Using a Circular Acoustic Emission Sensor Array," *Sensors (Basel),* vol. 16, no. 11, Nov 19 2016, doi: 10.3390/s16111951.

[43] P. Ulriksen, K. Haddad, and J. Spåls, "Acoustic Emission Detection and Source Location," Energiforsk, Report 2020:697, 2020, vol. 2020:697 issue 2020:697.

[44] M. Kharghani, K. Goshtasbi, M. Nikkah, and K. Ahangari, "Investigation of the Kaiser effect in anisotropic rocks with different angles by acoustic emission method," *Applied Acoustics,* vol. 175, 2021, doi: 10.1016/j.apacoust.2020.107831.

[45] M. Wu, D. Zhang, and C. Wang, "A novel deep penetrating eddy current probe based on phase shifted fields and its application to inspection of defects," *Metrology and Measurement Systems,* pp. 275–287, 2020, doi: 10.24425/mms.2020.132774.

[46] H. Shaikh *et al.*, "Use of eddy current testing method in detection and evaluation of sensitisation and intergranular corrosion in austenitic stainless steels," *Corrosion Science,* vol. 48, no. 6, pp. 1462–1482, 2006, doi: 10.1016/j.corsci.2005.05.017.

[47] C. Wang, M. Fan, B. Cao, B. Ye, and W. Li, "Novel Noncontact Eddy Current Measurement of Electrical Conductivity," *IEEE Sensors*

Journal, vol. 18, no. 22, pp. 9352–9359, 2018, doi: 10.1109/jsen.2018.2870676.

[48] L. Xie, A. L. Ribeiro, F. C. Alegria, and H. G. Ramos, "Detection of flaws in austenitic stainless steel plate using eddy current testing," *Research and Review Journal of Nondestructive Testing,* vol. 1, no. 1, 2023, doi: 10.58286/28556.

[49] M. Fan, B. Cao, P. Yang, W. Li, and G. Tian, "Elimination of liftoff effect using a model-based method for eddy current characterization of a plate," *NDT & E International,* vol. 74, pp. 66–71, 2015, doi: 10.1016/j.ndteint.2015.05.007.

[50] A. Berkache, J. Lee, and E. Choe, "Evaluation of Cracks on the Welding of Austenitic Stainless Steel Using Experimental and Numerical Techniques," *Applied Sciences,* vol. 11, no. 5, 2021, doi: 10.3390/app11052182.

[51] G. Niu, Y. Ji, W. Tang, and B. Zhang, "Defect Recognition for Eddy Current Testing of Spent Nuclear Fuel Canister using Convolutional Neural Network," presented at the 2023 IEEE 2nd Industrial Electronics Society Annual On-Line Conference (ONCON), 2023.

[52] A. Antony Jacob, S. Ravichandran, V. Upadhyay, P. Rajagopal, and K. Balasubramaniam, "Thickness Estimation of Marine Structures Using an ROV-Based Pulsed Eddy Current Technique," in *Advances in Non-destructive Evaluation*, (Lecture Notes in Mechanical Engineering, 2021, ch. Chapter 14, pp. 133–143.

[53] M. Smith and C. Laenen, "Inspection of nuclear storage tanks using remotely deployed ACFMT," (in English), *Insight,* vol. 49, no. 1, pp. 17–20, Jan 2007, doi: DOI 10.1784/insi.2007.49.1.17.

[54] W. Li, X. A. Yuan, G. M. Chen, J. H. Ge, X. K. Yin, and K. J. Li, "High sensitivity rotating alternating current field measurement for arbitrary-angle underwater cracks," (in English), *NDT & E International,* vol. 79, pp. 123–131, Apr 2016, doi: 10.1016/j.ndteint.2016.01.003.

[55] L. Wei, W. Ma, Q. Pan, D. Wen-jiao, X. a. Yuan, and X. Yin, "Detection and evaluation of weld defects in stainless steel using alternating current field measurement," presented at the AIP Conference Proceedings, 20 April, 2018.

[56] J. L. Shen, L. Zhou, H. Rowshandel, G. L. Nicholson, and C. L. Davis, "Determining the propagation angle for non-vertical surface-breaking cracks and its effect on crack sizing using an ACFM sensor," (in English), *Measurement Science and Technology,* vol. 26, no. 11, Nov 2015, doi: 10.1088/0957-0233/26/11/115604.

[57] P. Qi, H. Cui, M. Feng, W. Shao, S. Liao, and W. Li, "Preliminary study on detection technology of the cladding weld of spent fuel storage pool," 2018.

[58] X. a. Yuan *et al.*, "Recent development of alternating current field measurement technology for defects detection: A review," *NDT & E International,* vol. 155, 2025, doi: 10.1016/j.ndteint.2025.103430.

[59] W. Li, G. M. Chen, C. R. Zhang, and T. Liu, "Simulation analysis and experimental study of defect detection underwater by ACFM probe," (in English), *China Ocean Engineering*, vol. 27, no. 2, pp. 277–282, Apr 2013, doi: 10.1007/s13344-013-0024-x.

[60] W. Li, G. Chen, X. Yin, C. Zhang, and T. Liu, "Modeling and simulation of crack detection for underwater structures using an ACFM method," in *AIP Conference Proceedings*, 25 January 2013, vol. 1511, no. 1, pp. 436–440, doi: https://doi.org/10.1063/1.4789080.

[61] X. Yuan, Li, W., Zhao, J., Yin, X., Li, X., Zhao, J., "Visual Reconstruction of Irregular Crack in Austenitic Stainless Steel Based on ACFM Technique," in *Recent Development of Alternating Current Field Measurement Combine with New Technology*: Springer, Singapore, 2024.

[62] Y. A. Hsieh and Y. J. Tsai, "Machine Learning for Crack Detection: Review and Model Performance Comparison," (in English), *Journal of Computing in Civil Engineering*, vol. 34, no. 5, Sep 1 2020, doi: https://doi.org/10.1061/(ASCE)CP.1943-5487.0000918.

[63] X. Li, L. Xu, M. Wei, L. Zhang, and C. Zhang, "An underwater crack detection method based on improved YOLOv8," *Ocean Engineering*, vol. 313, 2024, doi: 10.1016/j.oceaneng.2024.119508.

[64] D. Chen, B. Huang, and F. Kang, "A Review of Detection Technologies for Underwater Cracks on Concrete Dam Surfaces," *Applied Sciences*, vol. 13, no. 6, 2023, doi: 10.3390/app13063564.

[65] Farmatome. "SUSI-Gen3 Submarine System." Farmatome. https://www.framatome.com/solutions-portfolio/portfolio/product/A0464/susi-robot-applications-visual-inspection-and-nde (accessed 08-15, 2025).

[66] T. Subsea. "Subsea NDT Applications." https://www.tscsubsea.com/# (accessed 08-15, 2025).

[67] Hausbots. "Hausbots." https://hausbots.com (accessed 10-07, 2025).

[68] D. Trekker. "Underwater ROVs." https://www.deeptrekker.com/products/underwater-rov#3-rov-comparison-chart-underwater-rov (accessed 08-15, 2025).

[69] VideoRay. "VideoRay Products." https://videoray.com/products (accessed 08-15, 2025).

[70] B. Robotics. "BlueROV2." https://bluerobotics.com/product-category/rov (accessed 08-15, 2025).

[71] E. Calculator. "Properties and Overview of Stainless Steel 304L." https://www.engineercalculator.com/metal-alloy-properties-and-overview/stainless-steel-304l-various-properties-and-overview/#:~:text=Stainless%20Steel%20304L%20Poissons%20Ratio,MPa%29%20240 (accessed 10-03, 2025).

[72] S. M. DataBase. "PRODUCT DATA of AISI 304L." https://www.spacematdb.com/spacemat/datasearch.php?name=AISI%20304L (accessed 10-03, 2025).

[73] P. A. Petcher and S. Dixon, "Mode mixing in shear horizontal ultrasonic guided waves," *Nondestructive Testing and Evaluation,* vol. 32, no. 2, pp. 113–132, 2016, doi: 10.1080/10589759.2016.1184268.

METHODS FOR LOCATING POOL LINER LEAKAGE AT NUCLEAR POWER PLANTS

This report evaluates practical methods for localizing leakage-relevant defects in thin stainless-steel pool liners in nuclear facilities, with particular emphasis on inspection under water. A state-of-the-art review is complemented by targeted EMAT shear-horizontal guided-wave experiments, which clarify detection mechanisms and practical limitations. Based on the combined findings, Alternating Current Field Measurement (ACFM) is identified as the most promising near-term technique for locating surface-breaking cracks, with Phased Array Ultrasonic Testing (PAUT) as a complementary method for detailed characterization. The results provide an application-oriented basis for prioritizing inspection techniques and guiding future development toward more reliable leakage localization with reduced downtime.

A new step in energy research

The research company Energiforsk initiates, coordinates, and conducts energy research and analyses, as well as communicates knowledge in favor of a robust and sustainable energy system. We are a politically neutral limited company that reinvests our profit in more research. Our owners are industry organisations Swedenergy and the Swedish Gas Association, the Swedish TSO Svenska kraftnät, and the gas and energy company Nordion Energi.

Energiforsk